

An ALMA spectroscopic survey of the *Planck* high-redshift object PLCK G073.4–57.5 confirms two protoclusters

Ryley Hill¹, Maria del Carmen Polletta^{2,3}, Matthieu Béthermin^{4,5}, Hervé Dole⁶, Rüdiger Kneissl^{7,8}, and Douglas Scott¹

¹ Department of Physics and Astronomy, University of British Columbia, 6225 Agricultural Road, Vancouver, V6T 1Z1, Canada

² INAF, Istituto di Astrofisica Spaziale e Fisica Cosmica Milano, Via A. Corti 12, I-20133 Milano, Italy

³ Department of Physics and Center for Astrophysics and Space Science, University of California at San Diego, 9500 Gilman Drive, La Jolla, CA 92093, USA

⁴ Laboratoire d'Astrophysique de Marseille, CNRS, LAM, Aix Marseille Université, 38 Rue Frédéric Joliot Curie, 13013 Marseille, France

⁵ Observatoire Astronomique de Strasbourg, CNRS, Université de Strasbourg, 11 Rue de l'Université, 67000 Strasbourg, France

⁶ Institut d'Astrophysique Spatiale, CNRS, Université Paris-Saclay, Bâtiment 121, 91405 Orsay, France

⁷ ESO Vitacura, European Southern Observatory, Alonso de Córdova 3107, Santiago, Chile

⁸ Joint ALMA Observatory, Alonso de Cordova 3107, Santiago, Chile

Received ...; accepted ...

ABSTRACT

Planck's High-Frequency Instrument observed the whole sky between 350 μm and 3 mm, discovering thousands of unresolved peaks in the cosmic infrared background. The nature of these peaks are still poorly understood – while some are strong gravitational lenses, the majority are spatial overdensities of star-forming galaxies, but with almost no redshift constraints. PLCK G073.4–57.5 (G073) is one of these *Planck*-selected peaks. G073 was previously observed by ALMA, with the results suggesting the presence of two structures (one around redshift 1.5 and one around redshift 2) aligned along the line of sight, but the results lacked robust spectroscopic confirmation. Characterizing the full redshift distribution of the galaxies within G073 is needed in order to better understand this representative example of these *Planck*-selected objects, and connect them to the emergence of galaxy clusters. We use ALMA Band 3 spectral scans to search for CO(3–2), CO(4–3), and C_I(1–0) line emission, targeting eight red *Herschel*-SPIRE sources in the field, as well as four bright SCUBA-2 sources. We find 15 emission lines in 13 galaxies, and using existing photometry information we secure the spectroscopic redshifts of all 13 galaxies. 11 of these galaxies are SPIRE-selected and lie in two structures at $\langle z \rangle = 1.53$ and $\langle z \rangle = 2.31$ (both with a standard deviation in redshift of 0.02), while the two SCUBA-2-selected galaxies are at $z = 2.61$. Using multiwavelength photometry we constrain stellar masses and star-formation rates, and using the CO and C_I emission lines we constrain gas masses. Our protocluster galaxies exhibit typical depletion timescales ($M_{\text{gas}}/\text{SFR}$) compared to field galaxies at the same redshifts, but enhanced gas-to-stellar mass ratios, potentially driven by emission line selection effects. We find that the two structures confirmed in our survey are reproduced in cosmological simulations of star-forming halos at high redshift; the simulated halos have a 60–70% probability of collapsing into galaxy clusters, implying that the two structures in G073 are genuinely protoclusters.

Key words. large-scale structure of Universe – Submillimetre: galaxies – Galaxies: star formation – Galaxies: clusters: general

1. Introduction

The Universe on the largest scales forms a ‘cosmic web’, with galaxy clusters at the intersections of the filaments (Bond et al. 1996). These are the largest gravitationally-bound objects in the Universe, and we believe that they play an important role on the evolution of the galaxies embedded within them because in the local Universe, cluster galaxies are more likely to be massive, red ellipticals with old stellar populations (e.g., Ellis et al. 1997; Andreon 2003; Muzzin et al. 2012). These observations effectively point to a process that primarily operates in galaxy clusters, where star formation produces massive elliptical galaxies early on, followed by a quenching phase.

Understanding how the large-scale environment led to a different star-formation process that resulted in such a stark differentiation between cluster galaxies and field galaxies is an

open question. Many models have been put forward; on the one hand, galaxies could experience accelerated growth through increased merger rates in overdense environments (e.g., Kauffmann 1996; Gottlöber et al. 2001; Fakhouri & Ma 2009), while on the other hand gas could be removed from galaxies as they travel through the intracluster medium (ICM) due to ram pressure stripping (e.g., Gunn & Gott 1972; Gavazzi et al. 2001; Boselli et al. 2019), or galaxies might be unable to accrete the new gas required to form more stars due to the hot ICM temperatures present in clusters (e.g., Larson et al. 1980; Balogh et al. 2000; Peng et al. 2015). To understand the contributions of these (and other) scenarios on galaxy evolution requires observations of cluster galaxies well before the cluster has fully virialized, which means finding examples of galaxy clusters early in their formation phase (i.e., protoclusters).

Protoclusters are now common in the literature, having been found in large Lyman- α surveys (e.g., Steidel et al. 2000; Chiang et al. 2015; Jiang et al. 2018), or around rare and extremely

Send offprint requests to: R. Hill
e-mail: ryleyhill@phas.ubc.ca

massive galaxies such as quasars (e.g., Dannerbauer et al. 2014; Noirot et al. 2018; Hennawi et al. 2015) and submillimetre (submm) galaxies (SMGs; e.g., Chapman et al. 2009; Casey et al. 2015; Oteo et al. 2018). However, such a diversity of selection techniques means that it is impossible to compare different protoclusters with one another and draw conclusions about overall populations.

Nonetheless, cosmic microwave background (CMB) experiments are now making progress towards large, uniform samples of protoclusters. CMB surveys operate at submm and millimetre wavelengths over very large areas, inevitably detecting the brightest extragalactic foreground objects (relative to the CMB), many of which are now known to be protoclusters (e.g., Flores-Cacho et al. 2016; Miller et al. 2018; Koyama et al. 2021; Polletta et al. 2021). In particular, *Planck* has identified over 2000 extragalactic objects with spectral energy distributions (SEDs) peaking between 350 and 850 μm (known as the *Planck* High- z Catalogue, or PHz; see Planck Collaboration XXXIX 2016), meaning that the emission is most likely thermal and originating from copious amounts of dust produced by elevated star-formation rates (SFRs) in galaxies shortly before they quench.

PLCK G073.4–57.5 (hereafter G073) is one such object. While G073 is not in the final PHz catalogue due to it being located just within the final Milky Way mask, it was part of a preliminary catalogue (with a less conservative mask) and was followed up with *Herschel*-SPIRE (Planck Collaboration XXVII 2015) and SCUBA-2 (MacKenzie et al. 2017). Following these observations, ALMA was used to observe eight red SPIRE sources in Band 6 (1 mm), detecting 18 galaxies in the continuum (Kneissl et al. 2019). While 18 mm-bright galaxies is already 8–30 times higher than expected from a random field distribution, the distribution of photometric redshifts suggested that the field contained overdensities around $z \approx 1.5$ and $z \approx 2$ (although with large uncertainties), while two bright lines were also serendipitously detected at the edge of one of the sidebands and later identified as CO(5–4) at $z = 1.5$, coinciding with the first peak in the photometric redshift distribution.

G073 therefore presents an opportunity to study overdense environments at a crucial epoch of cluster and galaxy formation. Around $z = 2$, galaxy clusters are beginning to virialize, and cluster galaxies often still have elevated SFRs compared to field galaxies (e.g., Hilton et al. 2010; Hayashi et al. 2011; Brodwin et al. 2013; Tran et al. 2015; Albers et al. 2016; Nantais et al. 2017; Mei et al. 2023). For most of these systems, the star-formation activity is significant down to the dense core region (e.g., Hilton et al. 2010; Hayashi et al. 2010; Tran et al. 2010; Fassbender et al. 2011; Tadaki et al. 2012). Since star formation will often heavily obscure a galaxy in dust, these key populations can be missed by optical observations, but long-wavelength observations of molecular gas lines (primarily CO) are completely unaffected. Furthermore, since the molecular gas is the main fuel for star formation, such observations can be used to trace gas masses and provide insight into the evolutionary state of cluster and protocluster galaxies. A small number of (proto)cluster galaxies have been observed in CO around $z = 2$, with some results suggesting higher gas fractions ($M_{\text{gas}}/M_{\text{star}}$) and shorter depletion timescales ($M_{\text{gas}}/\text{SFR}$) compared to field galaxies (e.g., Noble et al. 2017; Hayashi et al. 2018), while others do not find such a difference (e.g., Aravena et al. 2012; Rudnick et al. 2017).

The main issue to overcome is that our current observations are limited to only a few inhomogeneously-selected clusters and protoclusters. The PHz catalogue of over 2000 (uniformly-selected) protocluster candidates thus offers the opportunity to find statistically significant results with simple and understand-

able observational biases. To this end, in this paper we present a new ALMA survey of G073, searching for more $z = 1.5$ galaxies and spectroscopically confirming the redshift of the $z = 2$ structure. Ultimately, a full characterization of this object will help us understand how to carry out future studies of large samples of PHz objects.

This paper is arranged as follows. In Sect. 2 we describe our new ALMA observations and all ancillary data, in Sect. 3 we outline our data analysis pipeline, and in Sect. 4 we discuss how we derive physical properties. Section 5 presents our results, which we interpret in Sect. 6. The paper concludes in Sect. 7. Throughout this work we adopt a Chabrier (2003) initial mass function (IMF) and a flat Λ cold dark matter (ΛCDM) model with cosmological parameters $\Omega_{\Lambda} = 0.685$, $\Omega_{\text{M}} = 0.315$, and $H_0 = 67.4 \text{ km s}^{-1} \text{ Mpc}^{-1}$ (Planck Collaboration VI 2020).

2. Observations

2.1. Target selection

Our ALMA Band 4 survey targeted the eight red SPIRE sources (in eight separate pointings) previously followed up by ALMA in Cycle 2 (Kneissl et al. 2019). These eight targets form a complete sample of SPIRE sources found within the *Planck* beam and with colours satisfying $S_{350} / S_{250} > 0.7$ and $S_{500} / S_{350} > 0.6$, which is expected to filter out low- z interlopers. Since the ALMA primary beam is larger at 2 mm than at 1 mm, our observations covered all 18 galaxies detected by Kneissl et al. (2019). In addition to these eight SPIRE sources, we targeted the four highest signal-to-noise ratio (S/N) sources detected by SCUBA-2 at 850 μm (again within the *Planck* beam; see MacKenzie et al. 2017), bringing the total number of ALMA pointings to 12. The distribution of these pointings is shown in Fig. 1.

2.2. Cycle 6 ALMA observations

We received in total 3.23 hours of on-source observing time on G073 with ALMA in Cycle 6 (Project ID 2018.1.00562.S, PI R. Hill), taken in four executions on 2018 4, 8, 11, and 12 November. CO(5–4) and CO(2–1) were previously confirmed in galaxy ID 3 at $z = 1.5423$, so we tuned our Band 4 observations to centre the redshifted CO(3–2) line around 136 GHz in the lower sideband (LSB). The upper sideband (USB) was centred around 149 GHz in order to search for C_I(1–0) in the $z \approx 2$ structure and to measure dust continuum at 2.1 mm.

In the LSB data, the redshift range covered by CO(3–2) was 1.49–1.56, while in the USB data C_I(1–0) covered a redshift range of 2.23–2.34. The lower sideband could also contain CO(4–3) between $z = 2.32$ and $z = 2.41$, making a single line detection degenerate between the two expected structures; these situations are discussed on a case-by-case basis below. There are other potential contaminating lines such as CO(2–1) at $z < 0.7$ and higher- J lines at $z > 2.8$, which are strongly disfavoured given the photometric redshift distribution from Kneissl et al. (2019). There could additionally be C_I(1–0) in the lower sideband around $z \approx 2.6$, CO(3–2) in the upper sideband around $z \approx 1.3$, and CO(4–3) in the upper sideband around $z \approx 2.1$, but since multiple lines are detected in both the $z \approx 1.5$ and $z \approx 2$ structures (as shown below), we assume that there are only two redshift possibilities for all of the lines we detect. However for the SCUBA-2 targets we consider all possible redshifts because the original *Planck* selection would not have included objects bright at 850 μm .

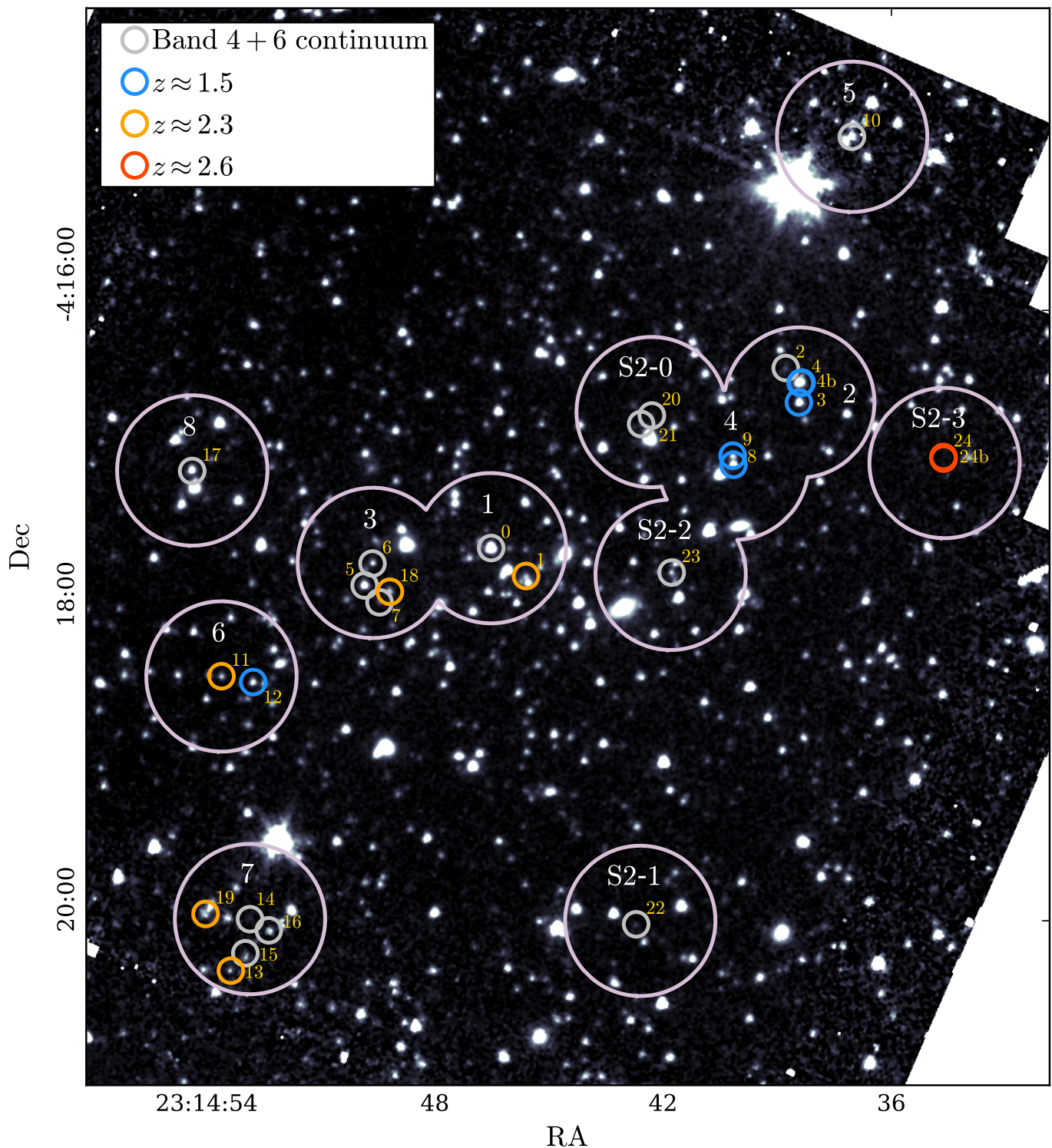


Fig. 1. Field of G073.4–57.5. In the background we show *Spitzer* 3.6- μm imaging, and the purple circles represent ALMA Band 4 follow-up pointings taken in Cycle 7. The ALMA pointings labelled 1 through 8 were also observed by ALMA in Band 6 in Cycle 2; these pointings were selected as bright, unresolved *Herschel*-SPIRE sources with red colours (see Kneissl et al. 2019). The ALMA pointings labelled S2-0 through S2-3 were selected as the highest S/N SCUBA-2 850 μm sources (see MacKenzie et al. 2017). Galaxies with only continuum detections in at least one of the ALMA Band 4 and 6 data are indicated by grey circles, while the galaxies in the $z \approx 1.5$ structure are shown as blue circles and galaxies in the $z \approx 2.3$ structure are shown as orange circles. The two SCUBA-2-selected galaxies for which we detected line emission are shown as red circles, tentatively assigned to $z = 2.6$ (see Sect. 3).

The Band 4 spectral set-up used four 1.78-GHz-wide continuum spectral windows (with channel widths of 15.6 MHz) around the central frequency of 143.1 GHz (2.1 mm). The spec-

tral windows were divided into the two receiver sidebands, separated by 12 GHz (i.e., their central frequencies were 136.1, 138.1, 148.1, and 150.1 GHz). 45–48 antennas were available

in the nominal C-5 array configuration with baseline lengths of 15–1400 m. This achieved synthesized beam sizes (using natural weighting) of around $0.65'' \times 0.55''$ (FWHM) in the lower side band and $0.58'' \times 0.50''$ in the upper sideband.

The observatory standard calibration was used. J0006–0623, a grid-monitoring source, was the bandpass and flux calibrator, with a flux density of 1.58 Jy at the central frequency. All pointings in the data sets shared the same phase calibrator, J2323–0317. The central continuum sensitivity in each of the 12 pointings was approximately $15\text{--}20 \mu\text{Jy beam}^{-1}$. The reduction was based on the calibration provided by the ALMA Pipeline using standard CASA tasks (CASA Team et al. 2022), using natural weighting and pixel sizes of $0.077''$.

2.3. Cycle 2 ALMA observations

In this paper we make use of existing ALMA observations of G073 taken in Cycle 2. These observations were presented in detail in Kneissl et al. (2019); briefly, G073 was observed for 0.4 hours in Band 6 using the standard Band 6 tuning centred at about 1.3 mm. A total of eight pointings were carried out, targeting the same eight *Herschel*-SPIRE-detected sources described above (see Fig. 1). Based on these initial observations, a total of 18 individual galaxies were detected in the continuum, while line emission was detected in two of the 18 galaxies (IDs 3 and 8).

2.4. Ancillary data

G073 has been observed in the near-infrared (NIR; $1.25 \mu\text{m}$ [J] and $2.15 \mu\text{m}$ [K_s]) with the Wide-field Infrared Camera (WIRCam) on the Canada France Hawaii Telescope and in the mid-infrared (MIR; $3.6 \mu\text{m}$ and $4.5 \mu\text{m}$) with IRAC on the *Spitzer* Space Telescope. The observations and the photometric data are described in Kneissl et al. (2019). The NIR and MIR counterparts and fluxes for two ALMA sources, IDs 4 and 15, have been revised because they were wrongly assigned to a foreground galaxy located about $1.1''$ and $1.6''$ from the millimetre-emitting sources, respectively. Since ID 4 is much fainter than the nearby source, it is not possible to obtain reliable flux estimates for it. This is also true at sub-mm/mm wavelengths where the SED is consistent with a low redshift (i.e., $z \approx 0.2$) source, suggesting that the nearby source dominates also at these wavelengths. The measured near and mid-IR flux densities S_J , S_{K_s} , $S_{3.6}$, and $S_{4.5}$ are listed in Table B.1.

3. Data Analysis

3.1. CO and C_I line search for protocluster galaxies

To conduct our line search in both the lower and upper sideband of our ALMA observations, we first used the publicly-available tool LineSeeker (González-López et al. 2017, 2019). This takes as input a primary beam-uncorrected data cube, and convolves the cube along the spectral axis with Gaussians of varying width, searching for significant peaks. The noise per channel is estimated iteratively by computing the standard deviation of all the pixels in a given channel, then recomputing the standard deviation of all the pixels whose absolute values are lower than 5 times the initial standard deviation. After convolution with a Gaussian of a given size, pixels whose spectra show peak S/N values above a chosen threshold are then returned to the user, and the procedure is repeated to search for pixels containing negative S/N peaks.

Table 1. Source properties.

Field	ID	RA Dec [J2000]	z	S_{2100} [mJy]
1	0	23:14:46.52 –4:17:33.4	...	<0.097
	1	23:14:45.60 –4:17:44.5	2.3060	0.325 ± 0.072
2	2	23:14:38.78 –4:16:22.6	...	0.225 ± 0.050
	3	23:14:38.43 –4:16:36.2	1.5424	0.122 ± 0.059
	4	23:14:38.36 –4:16:28.3	1.5390	<0.042
	4b	23:14:38.38 –4:16:28.6	1.5494	<0.034
3	18	23:14:49.18 –4:17:50.6	2.3370	<0.098
	5	23:14:49.85 –4:17:48.2	...	0.117 ± 0.042
	6	23:14:49.64 –4:17:39.5	...	<0.041
	7	23:14:49.45 –4:17:54.8	...	<0.129
4	8	23:14:40.15 –4:17:00.7	1.5125	0.203 ± 0.064
	9	23:14:40.17 –4:16:57.1	1.5055	<0.079
5	10	23:14:37.04 –4:14:51.7	...	<0.100
6	11	23:14:53.61 –4:18:23.9	2.3058	0.166 ± 0.042
	12	23:14:52.78 –4:18:26.1	1.5065	<0.073
7	13	23:14:53.36 –4:20:19.6	2.3395	0.129 ± 0.064
	14	23:14:52.86 –4:19:59.4	...	0.108 ± 0.038
	15	23:14:52.98 –4:20:12.8	...	<0.049
	16	23:14:52.37 –4:20:03.8	...	<0.044
	19	23:14:54.04 –4:19:57.3	2.2762	<0.055
8	17	23:14:54.38 –4:17:03.1	...	0.091 ± 0.035
	S2-0	20 23:14:42.29 –4:16:41.3	...	0.502 ± 0.062
	21	23:14:42.58 –4:16:44.7	...	0.421 ± 0.067
S2-1	22	23:14:42.71 –4:20:01.4	...	1.326 ± 0.098
S2-2	23	23:14:41.77 –4:17:43.1	...	0.174 ± 0.053
S2-3	24	23:14:34.63 –4:16:57.6	2.6127	0.377 ± 0.050
	24b	23:14:34.63 –4:16:58.3	2.6337	<0.061

We ran LineSeeker on all primary beam-uncorrected LSB and USB data cubes; for reference, the solid angle of each cube is about $0.76'$, while the bandwidth is about 3.5 GHz, corresponding to a velocity range of about 8000 km s^{-1} . We set the maximum width of the spectral convolution kernel to be 1000 km s^{-1} , which sets an upper limit to the width of line emission features in our search.

From the catalogues of positive and negative peaks returned by LineSeeker, we found that the most significant negative peak across all of the data cubes had an S/N of 6.1, thus we used this as our cutoff for identifying real positive peaks. There were a total of eight unique positive peaks in the LSB data with S/N values greater than 6.1; six of these peaks are spatially coincident with Band 6 continuum-detected galaxies from Kneissl et al. (2019), one peak is located in a field previously observed by ALMA but at a position with no continuum counterpart (ID 18), and one peak is in the S2-3 pointing (ID 24; see Fig. 1). Similarly, we found three unique positive peaks in the USB data above the S/N threshold, with two peaks coincident with a Band 6 continuum-detected galaxy, and one peak with no previously known counterpart (ID 19).

For completeness, we also placed $1.5''$ apertures around the previously-detected galaxies in G073 from Kneissl et al. (2019) with no line detections from LineSeeker. Since for these galaxies we have prior knowledge of their positions, we systematically search their spectra for fainter peaks down to 5σ (without any Gaussian convolution), but this did not return any additional lines.

Table 2. Properties of line detections.

Field	ID	Line	F [Jy km s ⁻¹]	L [10 ⁶ L _⊙]	L' [10 ⁹ K km s ⁻¹ pc ²]	FWHM [km s ⁻¹]
1	1	Ci(1–0)	1.22±0.26	68±15	17.8±3.9	580±100
2	3	CO(3–2)	2.38±0.10	45.6±1.9	34.4±1.4	420±17
	4	CO(3–2)	0.57±0.07	10.8±1.4	8.2±1.0	480±60
	4b	CO(3–2)	0.34±0.08	6.5±1.6	4.9±1.2	720±180
3	18	CO(4–3)	0.33±0.04	17.9±2.3	5.7±0.7	146±18
		Ci(1–0)	0.20±0.06	11.3±3.7	3.0±1.0	230±70
4	8	CO(3–2)	1.94±0.11	35.9±2.1	27.1±1.6	720±50
	9	CO(3–2)	0.35±0.06	6.4±1.1	4.8±0.8	320±50
6	11	Ci(1–0)	0.51±0.15	28.6±8.6	7.5±2.3	670±160
	12	CO(3–2)	1.28±0.12	23.4±2.1	17.7±1.6	570±50
7	13	CO(4–3)	0.52±0.08	27.9±4.1	8.9±1.3	218±32
		Ci(1–0)	0.15±0.08	8.7±4.5	2.3±1.2	140±40
	19	Ci(1–0)	0.99±0.12	54.2±6.3	14.2±1.6	340±50
S2-3	24	Ci(1–0)	0.49±0.11	33.6±7.6	8.8±2.0	470±100
	24b	Ci(1–0)	0.32±0.06	22.1±3.9	5.8±1.0	330±60

3.2. ALMA Band 4 continuum search

We also searched our primary beam-uncorrected data cubes for previously undiscovered (i.e., not reported in [Kneissl et al. 2019](#)) submm continuum sources. To do this, we calculated the noise-weighted mean of each pointing (LSB+USB), where the noise per channel was estimated as the standard deviation of all the pixels after masking out the 18 known galaxies from [Kneissl et al. \(2019\)](#), and obviously bright galaxies in our SCUBA-2 pointings. We searched each continuum map for both positive and negative S/N peaks, finding that the most significant negative peak across all twelve maps was 5.1. Following our line search, we set this as our continuum search threshold. This search did not yield any new detections in the pointings centred on the positions of the eight previous ALMA observations (fields 1 through 8), but in the four new pointings centred on SCUBA-2 sources, we detected five sources (one in fields S2-1, S2-2, and S2-3, and two in S2-0).

3.3. Redshifts, line measurements and continuum measurements

Our photometric catalogue of submm-detected galaxies in G073 consists of 11 galaxies with line detections, plus an additional 14 continuum-detected galaxies (detected in Band 4 or in Band 6) that may still be at a protocluster redshift, but whose line emission was too faint to be detected in our exposure. Here we outline the various Band 4 measurements made on this catalogue.

First, for each position in our catalogue, we create 3'' × 3'' continuum-subtracted cutouts in our Band 4 primary beam-corrected data cubes using the CASA task `imcontsub`. For the continuum subtraction, at each pixel we fit a 0th-order polynomial (i.e., a constant) across frequency space to the channels containing no line emission, and subtract the fit.

Next, we generate LSB and USB spectra for each galaxy using the continuum-subtracted data cubes by manually placing elliptical apertures at the positions returned by either our line search or our continuum search, and summing the pixels within the aperture. The radius and ellipticity of the apertures are set by the size of the 2σ contours in each cutout after calculating

the average over all available channels. For sources 4 (located in field 2) and 24 (located in field S2-3), two significant emission lines were detected in the spectrum. For both cases, averaging over the channels corresponding to each line, showed that the two moment-0 maps were spatially offset by about 0.5'', with one peak spatially coincident with the bright continuum source and the other having no continuum counterpart. We checked that there were no pairs of millimetre lines able to explain the two peaks assuming they came from the same galaxy (e.g. CO(7–6) and [Cii](2–1) around $z \approx 5$). We therefore classify the two secondary sources as companion galaxies (designated 4b and 24b), bringing the total number of line detections to 13. The resulting spectra are provided in Appendix A.

As discussed above, we assume that there are two possible CO transitions for the lines detected in the LSB, while the lines in the USB are Ci(1–0) at $z \approx 2.3$. To establish which CO transition we have observed, we note that for lines detected between about 137.8 and 139.1 GHz we would expect CO(4–3) in the LSB and Ci(1–0) in the USB; this is the case for five sources (IDs 8, 9, 12, 13, and 18). For these sources, while Ci(1–0) was not detected in the USB with S/N > 6.1, lines are still possible at a lower significance. We note that CO(4–3) typically has a peak flux density brighter by a factor of 2 compared to Ci(1–0) in SMGs (e.g., [Birkin et al. 2021](#); [Hagimoto et al. 2023](#)), while for each of these sources the line detected in the LSB has a peak flux density about 3–5 times the spectrum rms.

We therefore perform a likelihood ratio test. We first fit a single Gaussian with three free parameters (amplitude, mean, and standard deviation) to the LSB line and calculate the likelihood function (here given by $\mathcal{L} = \exp(-\chi^2/2)$). We then perform a second fit for two Gaussians, where only the amplitude of the second Gaussian is a free parameter as the mean is fixed to the expected frequency of Ci(1–0) and the standard deviation is fixed to be equal to the first Gaussian. We recalculate the likelihood function, and then calculate $\Delta\mathcal{L} = 2(\log \mathcal{L}_2 - \log \mathcal{L}_1)$. The difference in degrees of freedom between the models is 1, so $\Delta\mathcal{L}$ is expected to follow a χ^2 distribution with 1 degree of freedom and the relevant statistic (t) is the χ^2 survival function (or 1 minus the cumulative distribution function) evaluated at $\Delta\mathcal{L}$. This statistic can be interpreted as the probability that the null hypothesis

esis (in this case the model with one Gaussian) describes the data better than the alternative, and so we apply a threshold of 0.05 below which we reject the null hypothesis.

We find that we cannot reject the null hypothesis for IDs 8, 9, and 12 ($t = 0.77$, $t = 1.00$, and $t = 0.99$, respectively), thus we interpret the line emission as CO(3–2). For IDs 13 and 18 we reject the null hypothesis with $> 95\%$ confidence ($t = 0.038$ and $t = 2.3 \times 10^{-5}$, respectively), so we assume that we have detected both CO(3–2) and C_I(1–0). [Kneissl et al. \(2019\)](#) discussed a tentative (S/N ≈ 3) CO(5–4) line detection in ID 8 at $z = 1.545$, but the CO(3–2) line we have identified with an S/N of about 17 places this galaxy at $z = 1.513$ – we conclude that the possible CO(5–4) line was in fact a noise excursion.

For IDs 4 and 24 (plus their companion galaxies) the line emission is observed at a frequency where we cannot perform this test. ID 4 (and its companion 4b) happens to lie behind a large $z < 0.5$ foreground galaxy and therefore we do not have good near-IR continuum measurements, thus we just assume that it is at the same redshift as ID 3. For ID 24 we fit the available near-IR and mm continuum photometry to a range of possible redshifts assuming the detected line is CO(3–2), CO(4–3), and C_I(1–0), then calculate χ^2 for each fit. We find that a redshift of 2.6, corresponding to the C_I(1–0) line, minimizes χ^2 , so we adopt this as the redshift of this galaxy and its companion. Lastly, the line detected at the location of ID 3 is unambiguously CO(3–2), since two other CO lines have previously been detected.

For the 13 galaxies with line emission, we fit single Gaussian functions to the observed lines in order to estimate various line properties. From the fit, line strengths/luminosities are estimated by summing all channels within $\pm 3\sigma$ of the mean of the fit, while the line FWHM are taken directly from the standard deviation of the fit, and redshifts are calculated using the mean of each fit. The line luminosities are calculated in L' units following [Solomon et al. \(1997\)](#) as

$$L'_{\text{line}} = \frac{c^2}{2k} S (\Delta V) \nu_{\text{obs}}^{-2} D_L^2 (1+z)^{-3}, \quad (1)$$

where $S (\Delta V)$ is the line intensity derived from the Gaussian fit, ν_{obs} the observed frequency of the line (see [Table 1](#)) and D_L is the usual cosmological luminosity distance. We also calculate the line luminosities in solar luminosity units following the same integration range.

Following this, continuum flux densities are calculated using the same apertures by averaging over all of the channels outside the $\pm 3\sigma$ range, or for galaxies with no line emission detected, by averaging over all of the available Band 4 channels. Since many of the galaxies in our catalogue come from detections in Band 6 data, we are effectively performing forced aperture photometry at these positions of interest; therefore, we set a low continuum flux density S/N threshold of 2 for our continuum detections. We find that we are able to measure Band 4 continuum flux densities above this level in eight out of the 18 galaxies reported [Kneissl et al. \(2019\)](#), with an additional five continuum flux density detections coming from new galaxies.

The results are summarized in [Tables 1 and 2](#). In [Appendix A](#) we provide spectra and moment-0 maps (where lines are detected) for all of the galaxies in the sample.

4. Physical properties of protocluster galaxies

4.1. Stellar masses and star-formation rates

We estimate the stellar mass of the line-detected sources by modelling their SEDs with the Code Investigating GALaxy Emission

(CIGALE; [Boquien et al. 2019](#)). This code models galaxy SEDs using stellar and dust components, and offers the advantage of modelling simultaneously the NIR part of the SED and the sub-mm/mm emission in a self-consistent way by preserving the energy balance between the stellar radiation that is absorbed by the dust and its re-emission at longer wavelengths (see [Buat et al. 2019](#) for a discussion on this assumption).

For the reference model, we assumed a delayed star-formation history (SFH) with an optional burst, a [Chabrier \(2003\)](#) initial mass function (IMF), the stellar population models of [Bruzual & Charlot \(2003\)](#), the dust models from [Draine et al. \(2014\)](#), the [Calzetti et al. \(2000\)](#) attenuation law, and solar metallicity ($Z = 0.02$). The best-fit is assessed through χ^2 , and the best-fit parameters and associated uncertainties are estimated as the likelihood-weighted means and standard deviations. The CIGALE best-fit models, available for seven out of nine CO-emitters with available NIR photometry, are shown in [Fig. 2](#). The stellar masses and SFRs (instantaneous, SFR_{inst} , and averaged over the past 100 Myrs, SFR_{100}) derived from the CIGALE best-fits are reported in [Table 3](#). We also derive SFR_{IR} , the SFR from the total IR luminosity (L_{IR}) assuming the relation in [Kennicutt & Evans \(2012\)](#) corrected for a Chabrier IMF (i.e., $\text{SFR}_{\text{IR}} = 1.40 \times 10^{-10} \times L_{\text{IR}}$; see [Table 3](#)). The IR luminosity (L_{IR}) was obtained from fitting the sub-mm/mm data with a modified blackbody using the `cmcirsed` package ([Casey 2012](#)), and assuming the CO-derived redshift and a dust emissivity-index β equal to 1.8 ([Cortese et al. 2014](#); [Pokhrel et al. 2016](#)). Since SFR_{inst} and SFR_{100} can differ significantly, by up to a factor of 3, we use SFR_{IR} in the following because it is usually intermediate between the two values provided by the CIGALE best fit. In addition, it is directly comparable with the values reported in the literature where it is commonly used, in particular for mm-selected galaxies. Compared to SFR_{IR} , SFR_{inst} can be twice as high, and SFR_{100} four times smaller. We note that [Kneissl et al. \(2019\)](#) estimated the SFRs for the same galaxy sample using the same `cmcirsed` package; however, they lacked spectroscopic redshifts and the additional 2-mm flux densities (S_{2000}). Nonetheless, we find comparable results.

In [Fig. 3](#) we show the offset from the average star-forming main-sequence (MS) as parameterized by [Popesso et al. \(2023\)](#) using each source's redshift and stellar mass. The grey shaded region corresponds to the scatter of 0.3 dex around the MS. Following [Rodighiero et al. \(2011\)](#), we classify a source as a starburst if the SFR is four times higher than expected according to the MS for a galaxy with the same stellar mass and at the same redshift, and as a normal SFG if the SFR is lower than this threshold. Four G073 sources (IDs 1, 8, 12, and 24) are considered starbursts based on the MS offset and the remaining six are consistent with the MS. In the figure, we also show the position of CO-detected cluster and protocluster members at $1.40 < z < 2.65$ from the literature (see the caption for detailed references). Compared to other clusters at similar redshifts, the G073 sources are on average more star-forming, but sources with similarly high SFRs are observed in other structures.

4.2. Molecular gas masses

Molecular gas masses are derived from CO luminosities using a single scaling factor as

$$M_{\text{gas}}^{\text{CO}} = \alpha_{\text{CO}} L'_{\text{CO}(1-0)}, \quad (2)$$

Table 3. Physical properties derived from line detections and CIGALE.

ID	z	M_{star} ($10^{10} M_{\odot}$)	SFR_{inst} ($M_{\odot} \text{ yr}^{-1}$)	SFR_{100} ($M_{\odot} \text{ yr}^{-1}$)	SFR_{IR}	$M_{\text{gas}}^{\text{CO}}$ ($10^9 M_{\odot}$)	$M_{\text{gas}}^{\text{CI}}$ ($10^9 M_{\odot}$)	μ_{gas}	τ_{depl} (Gyr)	$\text{SFR}/\text{SFR}^{\text{MS}}$	$\tau_{\text{depl}}/\tau_{\text{depl}}^{\text{MS}}$	$\mu_{\text{gas}}/\mu_{\text{gas}}^{\text{MS}}$
1	2.3060	8.9±3.6	609±84	280±48	442 ⁺⁴⁸ ₋₄₂	...	404±86	4.52±2.07	0.91±0.22	4.6±0.5	1.9±0.4	5.4±2.5
3	1.5424	7.8±0.5	301±21	172±9	174 ⁺¹⁴ ₋₁₄	237±10	...	3.06±0.26	1.37±0.12	3.2±0.3	2.3±0.2	4.9±0.4
4	1.5390	331 ⁺²⁵ ₋₂₃	57±7
4b	1.5494	34±8
18	2.3370	11.6±1.7	116±92	102±32	...	72±9	68±20	0.62±0.12	0.62±0.50	1.1±0.8	1.4±1.1	0.9±0.2
8	1.5125	5.4±1.1	873±102	264±33	609 ⁺⁶³ ₋₅₇	186±11	...	3.48±0.75	0.31±0.03	13.4±1.3	0.5±0.1	4.6±1.0
9	1.5055	6.4±1.2	54±19	52±7	47 ⁺¹⁶ ₋₁₃	33±6	...	0.52±0.13	0.72±0.26	1.0±0.3	1.1±0.4	0.8±0.2
11	2.3058	10.0±3.3	245±233	136±66	120 ⁺⁸⁴ ₋₅₀	...	169±50	1.69±0.76	1.41±0.90	1.2±0.7	3.0±1.9	2.1±1.0
12	1.5065	2.7±0.7	400±51	131±22	240 ⁺³² ₋₂₉	122±11	51±27	4.44±1.19	0.51±0.08	7.4±0.9	0.6±0.1	4.1±1.1
13	2.3395	4.4±1.9	360±91	154±35	237 ⁺²⁵ ₋₄₉	114±17	...	2.59±1.18	0.48±0.13	3.3±0.8	0.8±0.2	2.0±0.9
19	2.2762	8.6±1.1	86±58	76±23	320±39	3.73±0.66	3.73±2.56	0.9±0.6	7.6±5.2	4.4±0.8
24	2.6127	2.2±1.6	194±95	77±35	413 ⁺¹⁰⁸ ₋₈₆	...	201±45	9.23±7.10	0.49±0.16	7.8±1.8	0.6±0.2	4.1±3.2
24b	2.6337	133±25

Notes. Source IDs in boldface are classified as starbursts based on the main-sequence offset. The stellar mass (M_{star}), the instantaneous star-formation rate (SFR_{inst}) and the SFR averaged over the past 100 Myr (SFR_{100}) were obtained from the CIGALE SED best-fit model (see Sect. 4). The CIGALE parameters are not available for IDs 4, 4b, and 24b because they are not detected in the NIR and MIR images. SFR_{IR} was derived from the total IR luminosity (L_{IR}) assuming the relation in Kennicutt & Evans (2012) corrected for a Chabrier IMF (i.e., $\text{SFR} = 1.40 \times 10^{-10} \times L_{\text{IR}}$) and L_{IR} was obtained from fitting the sub-mm/mm data with a modified blackbody using the cmcirsed package (Casey 2012). SFR_{IR} was not derived for IDs 4b, 18, 19, and 24b because of lack of submm/mm detections. The molecular gas mass, $M_{\text{gas}}^{\text{CO}}$, was derived from $L'_{\text{CO}(1-0)}$ assuming $\alpha_{\text{CO}} = 4.36 M_{\odot} \text{ pc}^{-2} (\text{K km s}^{-1})^{-1}$ (Bolatto et al. 2013; Genzel et al. 2015), and $M_{\text{gas}}^{\text{CI}}$ as $5.2 \alpha_{\text{CO}} L'_{\text{CI}(1-0)}$ (Birkin et al. 2021). The gas-to-stellar mass ratio is given by $\mu_{\text{gas}} = M_{\text{gas}}/M_{\text{star}}$, and the gas depletion time by $\tau_{\text{depl}} = M_{\text{gas}}/\text{SFR}_{\text{IR}}$ (here we use CO-derived gas masses when both CO and CI are available). The main sequence offset ($\text{SFR}/\text{SFR}^{\text{MS}}$) is derived using SFR_{IR} , or SFR_{inst} when the former is not available (i.e., for IDs 18 and 19), and the SFR predicted by the relation in Popesso et al. (2023) assuming the redshift and the stellar mass of each source. The relative quantities $\tau_{\text{depl}}/\tau_{\text{depl}}^{\text{MS}}$ and $\mu_{\text{gas}}/\mu_{\text{gas}}^{\text{MS}}$ are derived by assuming the scaling relations for $\mu_{\text{gas}}^{\text{MS}}$ and $\tau_{\text{depl}}^{\text{MS}}$ as a function of stellar mass and redshift from Liu et al. (2019).

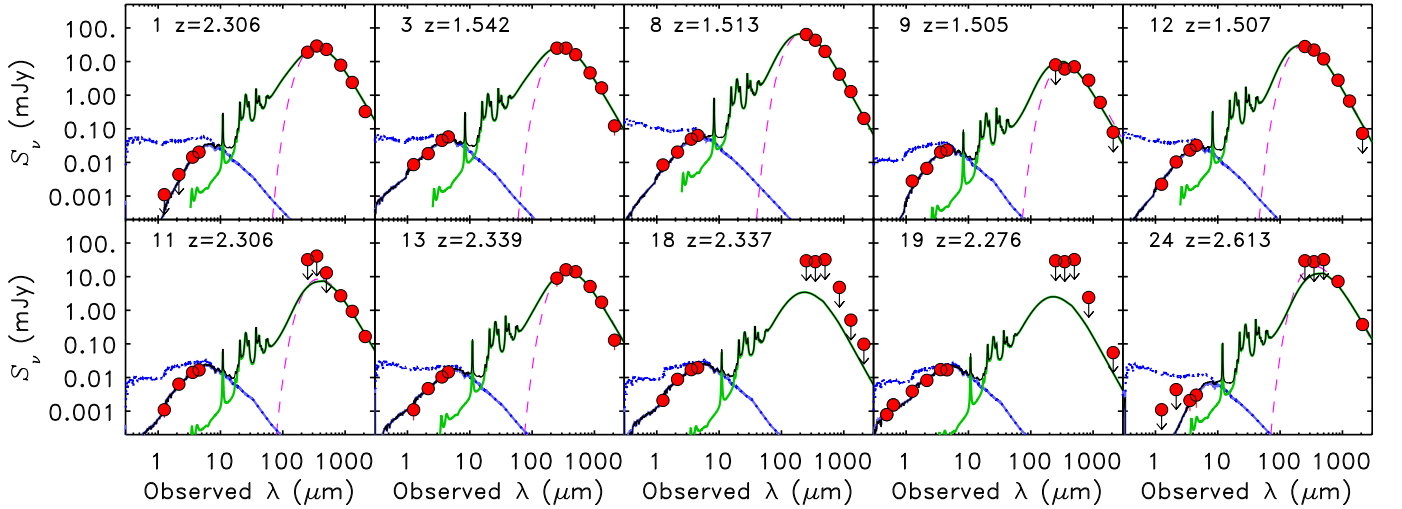


Fig. 2. Near-IR-through-mm SEDs (CFHT/WIRCam, *Spitzer*/IRAC, *Herschel*/SPIRE, SCUBA-2, and ALMA at 1.3 and 2.2 mm) of the sources with line detections (full red circles). Downward arrows are 5σ upper limits. The CIGALE best-fit model is shown with a black solid line. The blue dotted line shows the stellar light before dust attenuation, and the solid blue line shows the attenuated stellar light. The green line shows the dust component. The best-fit modified blackbody model to the submm/mm data is shown with a magenta dashed line. The source identifier is annotated and listed in Table 3.

where α_{CO} is the scaling parameter. To derive gas masses from CI we use a similar equation, namely

$$M_{\text{gas}}^{\text{CI}} = \alpha_{\text{CI}} L'_{\text{CI}(1-0)}. \quad (3)$$

We note that since we have not observed the CI(2–1) transition, we cannot take into account the gas excitation temperature, which is commonly used to calculate the partition function

and obtain gas mass estimates with less uncertainty (e.g., Bothwell et al. 2017; Dunne et al. 2021; Gururajan et al. 2023). This simple parameterization was calibrated using a large sample of SMGs with both CI(1–0) and CO(4–3) detections by Birkin et al. (2021), finding an average $\alpha_{\text{CI}}/\alpha_{\text{CO}}$ of 5.2 ± 1.3 , which we use here.

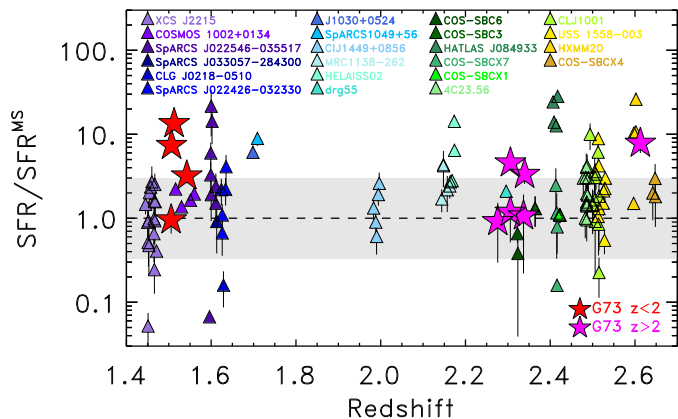


Fig. 3. Offset from the main sequence of star formation (Popesso et al. 2023) as a function of redshift. The grey region represents 0.5 dex scatter around the main sequence. Filled stars show the CO-emitters in G073 with a stellar mass estimate (red are those with $z < 2$ and magenta those with $z > 2$). Coloured triangles represent CO-detected cluster and protocluster members from the literature at $1.4 < z < 2.65$: XCS J2215 at $z = 1.46$ from Hayashi et al. (2018); COSMOS 1002+0134 at $z = 1.55$ from Aravena et al. (2012); SpARCS J022546–035517 at $z = 1.59$ from Noble et al. (2019); SpARCS J033057–284300 at $z = 1.613$ from Noble et al. (2017); CLG J0218–0510 at $z = 1.613$ from Rudnick et al. (2017); SpARCS J022426–032330 at $z = 1.613$ from Noble et al. (2017); J1030+0524 at $z = 1.694$ from D’Amato et al. (2020, 2021); SpARCS1049+56 at $z = 1.710$ from Webb et al. (2015); CIJ1449+0856 at $z = 1.990$ from Coogan et al. (2018); MRC1138–262 at $z = 2.160$ from Dannerbauer et al. (2017); Tadaki et al. (2019); HELAISS02 at $z = 2.171$ from Gómez-Guijarro et al. (2019); DRG55 at $z = 2.290$ from Chapman et al. (2015); COS–SBC6 at $z = 2.233$; COS–SBC3 at $z = 2.365$ from Sillassen et al. (2024); HATLAS J084933 at $z = 2.410$ from Ivison et al. (2013); COS–SBCX7 at $z = 2.415$; COS–SBCX1 at $z = 2.422$ from Sillassen et al. (2024); 4C23.56 at $z = 2.490$ from Tadaki et al. (2019); Lee et al. (2017); CLJ1001 at $z = 2.510$ from Wang et al. (2018); USS 1558–003 at $z = 2.530$ from Tadaki et al. (2014, 2019); HXMM20 at $z = 2.602$ from Gómez-Guijarro et al. (2019); COS–SBCX4 at $z = 2.646$ from Sillassen et al. (2024).

With this calibration, the only conversion factors we need to assume are α_{CO} and the scaling of the various CO luminosities to $L'_{\text{CO}(1-0)}$: α_{CO} can range from around 0.2 to $10 M_{\odot} \text{pc}^{-2} (\text{K km s}^{-1})^{-1}$ (Tacconi et al. 2008; Casey et al. 2014), depending on the physical properties of the galaxy such as metallicity (Genzel et al. 2012, 2015; Amorín et al. 2016; Tacconi et al. 2018; Inoue et al. 2021) or SFR, with respect to that expected for a galaxy with the same stellar mass and redshift on the main sequence (MS) relation (see equation 2 in Castignani et al. 2020). Galaxies above the MS, like starburst galaxies, can have smaller α_{CO} values than those on the MS. Similarly, galaxies with lower metallicities can have smaller α_{CO} values. The α_{CO} –metallicity relation is, however, valid only for massive ($M_{\text{star}} > 10^{10} M_{\odot}$) SFGs (Genzel et al. 2015). For the galaxies in G073 with $M_{\text{star}} > 10^{10} M_{\odot}$ the derived α_{CO} values range from 4.0 and 6.7 (Genzel et al. 2015; Tacconi et al. 2018). To be consistent with previous works, we adopt a conservative $\alpha_{\text{CO}} = 4.36 M_{\odot} \text{pc}^{-2} (\text{K km s}^{-1})^{-1}$ (Bolatto et al. 2013; Genzel et al. 2015) for all sources, independent of their MS-based classification. This α_{CO} conversion factor is commonly used for the Milky Way and for normal SFGs with solar metallicities (Bolatto et al. 2013; Genzel et al. 2015), and it includes a correction factor for helium. Regardless of the choice of α_{CO} , there are large systematic uncertainties involved in estimating the gas mass, which we ignore here for simplicity.

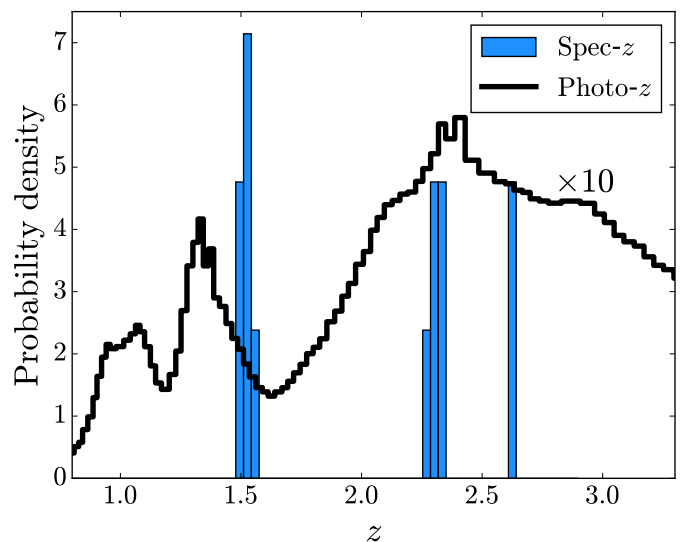


Fig. 4. Distribution of the 13 spectroscopic redshifts found in our ALMA survey, compared to the total photometric redshift distribution of all 18 continuum-selected galaxies in Kneissl et al. (2019). The photometric redshift distribution has been scaled by a factor of 10 to more easily compare with the spectroscopic redshift distribution.

As a last step, the measured CO luminosities are converted to CO(1–0) luminosities, $L'_{\text{CO}(1-0)}$, using the $L'_{\text{CO}(3-2)}$ and $L'_{\text{CO}(4-3)}$ to $L'_{\text{CO}(1-0)}$ ratios $r_{3,1} = 0.60 \pm 0.11$ and $r_{4,1} = 0.32 \pm 0.05$ (Birkin et al. 2021). The derived gas masses are listed in Table 3.

5. Results

5.1. Redshift distribution

In Fig. 4 we show the distribution of the 13 galaxy redshifts we have detected in our ALMA survey, alongside the photometric redshift probability distributions originally determined for the 18 galaxies from Kneissl et al. (2019). The two structures initially predicted by Kneissl et al. (2019) at $z \approx 1.5$ and $z \approx 2$ are seen as the two broad peaks in the probability distribution, and the redshifts we have spectroscopically confirmed agree with these two peaks. For the $z \approx 1.5$ structure, we find six galaxies with an average redshift of $z = 1.526$, while for the $z \approx 2$ structure we find five galaxies (ignoring the SCUBA-2 galaxies) with an average redshift of $z = 2.313$. Evidently none of the SCUBA-2 sources we have targeted are within the structures identified by *Planck* and *Herschel*, which we discuss further below.

Figure 5 shows the spatial distribution of the two structures, colour-coded according to their line-of-sight velocity relative to the mean redshift of each group. We find that most of the $z = 1.5$ galaxies are spatially concentrated in the north-west corner of the field-of-view initially defined by the *Planck* beam, while the $z = 2.3$ galaxies are concentrated in the south-east corner, about $1'$ from the lower-redshift structure. This distribution points to the conclusion that the original *Planck* data has selected an area on the sky where two protoclusters are aligned along the line of sight to within about $3'$ of one-another, relative to the $5'$ *Planck* beam.

5.2. Depletion timescales

The depletion timescale is given by $\tau_{\text{depl}} = M_{\text{gas}}/\text{SFR}$ (thus it has units of time), which provides a crude estimate for how long it

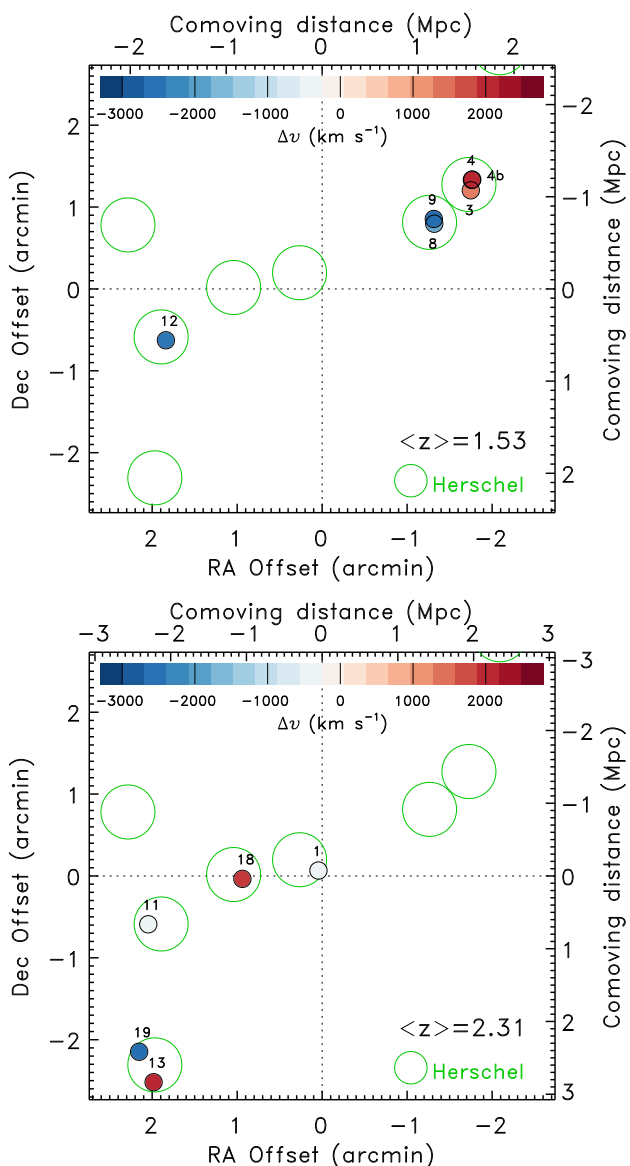


Fig. 5. Spatial distribution of the CO-detected sources at $1.50 < z < 1.55$ (top panel) and at $2.27 < z < 2.34$ in the G073.4–57.5 field (full circles) with colour corresponding to the redshift offset from the average value of $\langle z \rangle = 1.53$ and 2.31 , respectively, expressed in terms of velocity offset as indicated by the horizontal bar on the top. Large green circles represent the positions of the *Herschel* sources in the field.

would take a galaxy to convert all of its gas into stars, assuming the SFR remains constant. We therefore plot the molecular gas mass versus the SFR in Fig. 6, along with lines of constant depletion time and the relations that describe normal SFGs, as parameterized by Sargent et al. (2014).

We also show for comparison the values of the CO-detected cluster and protocluster galaxies described in Sect. 4.1. The gas masses from the literature have been derived from various CO transitions and α_{CO} values – e.g., $\alpha_{\text{CO}} = 4.36$ in Noble et al. (2017, 2019); Rudnick et al. (2017), $\alpha_{\text{CO}} = 0.8$ in Ivison et al. (2013) – and in some cases a stellar mass-dependent correction was applied resulting in final α_{CO} values ranging from 4.16 to 6.09 (Hayashi et al. 2018).

The conversion factor adopted by Sargent et al. (2014) varies with the metallicity following Wolfire et al. (2010) and is 4.4 at solar metallicity and always above 3. The gas masses in Liu et al.

(2019) are derived from the continuum. We corrected all the gas mass estimates from this literature cluster sample to have the same α_{CO} conversion factor of 4.36 (when possible), which is the value we used for G073. The scaling relations used to represent normal star-forming galaxies in the field are consistent with the adopted conversion.

We find that the depletion timescales of the G073 CO emitters are scattered around the values observed in normal SFGs ($0.3 < \tau_{\text{depl}}/\text{Gyr} < 3.71$). The median depletion times for the G073 sources and for the cluster members are (0.7 ± 0.6) Gyr and (0.8 ± 1.2) Gyr, respectively, thus we find no significant difference.

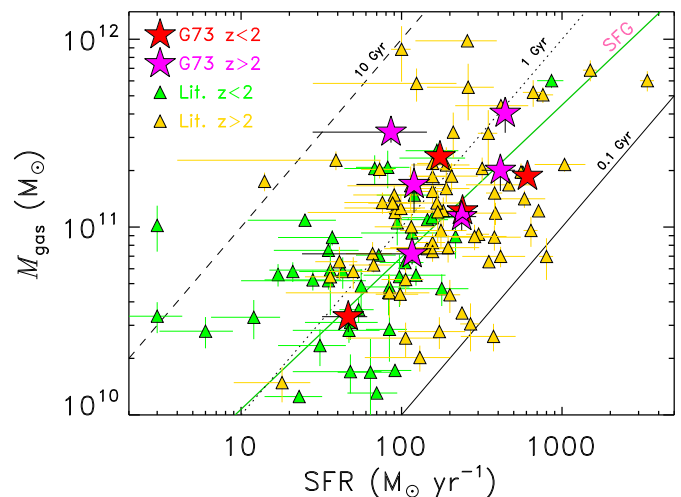


Fig. 6. Molecular gas mass as a function of SFR for the G073 sources (full stars, red for $z < 2$ and magenta for $z > 2$). Small filled triangles represent cluster and protocluster members from the literature from Fig. 3 (yellow triangles, $1.4 < z < 2$; green triangles, $2.0 < z < 2.65$). The solid green lines represent the average relation for normal SFGs (Sargent et al. 2014). The black lines represent constant gas depletion times (solid, 0.1 Gyr; dotted, 1 Gyr; and dashed, 10 Gyr).

5.3. Gas-to-stellar mass ratio

The gas-to-stellar mass ratio, defined as $\mu_{\text{gas}} = M_{\text{gas}}/M_{\text{star}}$, is of interest because it provides insight into the fraction of baryonic matter available to be converted to stars. In the limit where a galaxy does not accrete additional gas throughout its lifetime, the gas-to-stellar mass ratio is a crude estimate of a galaxy’s maturity. Figure 7 shows the gas masses as a function of stellar masses for the galaxies in G073, along with the CO-detected cluster and protocluster galaxies from the literature and the scaling relations expected for field galaxies from Liu et al. (2019). We also include several curves of constant gas-to-stellar mass ratio for reference.

Our sample of galaxies in G073, along with a collection from the literature, mostly lies above the field galaxy curve. Quantitatively, the G073 sample has a median gas-to-stellar mass ratio of $\mu_{\text{gas}} = 3.5^{+3.1}_{-1.6}$, while our comparison sample has a median gas-to-stellar mass ratio of $\mu_{\text{gas}} = 1.6^{+2.3}_{-0.9}$. This is contrary to what we might have expected given the higher SFRs of our sample; according to the MS, higher SFRs should lead to higher stellar masses, and therefore lower gas-to-stellar mass ratios. Since the opposite is observed in our case, the relatively high SFRs must be compensated by relatively high gas masses. Again, this might be a selection effect due to the fact that our CO survey is sen-

sitive to galaxies with the highest gas masses (we discuss this possibility more in Sect. 6).

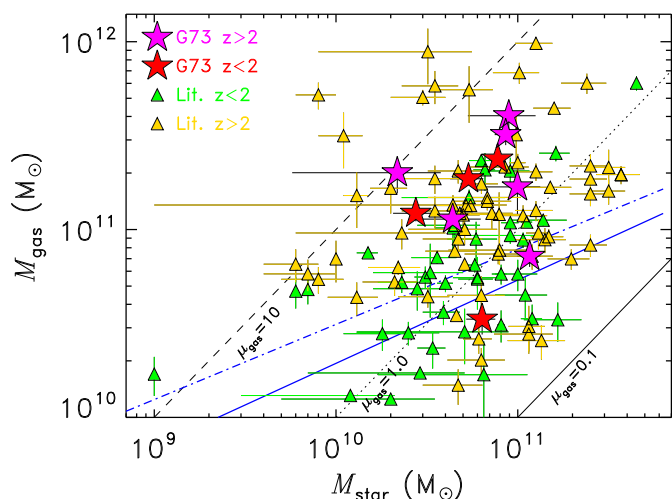


Fig. 7. Gas mass of the galaxies in G073 as a function of stellar mass. Symbols are as in Fig. 6. The solid, dotted and dashed black lines represents $\mu_{\text{gas}} = M_{\text{gas}}/M_{\text{star}} = 0.1, 1.0,$ and $10,$ respectively. The solid and dot-dashed blue lines represent the scaling relations from Liu et al. (2019) at $z = 1.53,$ and $2.3,$ respectively.

6. Discussion

6.1. The large-scale structure probed by G073

The primary result of our ALMA survey of G073 is the spectroscopic confirmation of two protoclusters within a single PHZ object, one at $z = 1.53,$ and the other at $z = 2.31.$ These two overlapping structures were initially suggested by Kneissl et al. (2019) based on photometric redshifts with large uncertainties, but now with improved knowledge of the systems we can further understand the nature of this PHZ object (and hence others), including using simulations.

Gouin et al. (2022) compared the $z \approx 1.5$ and $z \approx 2$ structures in G073 to the $(300 \text{ Mpc})^3$ TNG300 simulation using primarily photometric redshift data from Kneissl et al. (2019); at the time, only two galaxies had spectroscopic redshifts around $z \approx 1.5$ (IDs 3 and 8, although the redshift for ID 8 has been updated by our new observations). Gouin et al. (2022) identified three additional galaxies as being part of the $z \approx 1.5$ based on their photometric redshifts (IDs 5, 6, and 12), but we have instead found that IDs 4, 9, and 12 are in this structure. At $z \approx 2$ they identified IDs 1, 11, 13, 14, and 15, whereas we found IDs 1, 11, 13, 18, and 19 are in the structure. The handful of misidentified galaxies reflects the uncertain nature of photometric redshifts, although the discrepancy is not particularly large.

For the simulation comparison, Gouin et al. (2022) chose the redshift snapshot closest to the actual redshifts of the G073 structures, selected 30 of the most star-forming halos (defined to include all gas cells in a friends-of-friends group), then accounted for observational biases by including galaxies within a cylinder (centered on a given star-forming halo) with a diameter of $2.4'$ and a length encompassing ± 0.17 in redshift for the $z \approx 1.5$ structure, and ± 0.26 in redshift for the $z \approx 2$ structure. Lastly, an SFR cut of $30 M_{\odot} \text{ yr}^{-1}$ was applied to the galaxies within the simulated cylinders. This is comparable to our observational sensitivity – our 5σ line luminosity threshold is about $0.3 \text{ Jy km s}^{-1},$

corresponding to a gas mass of $3 \times 10^{10} M_{\odot}$ (assuming CO(3–2) at $z = 1.5$) or a SFR of $30 M_{\odot} \text{ yr}^{-1}$ using the scaling relation from Sargent et al. (2014). For C_I(1–0) at $z = 2.3,$ this limit corresponds to a gas mass of $10 \times 10^{10} M_{\odot},$ or a SFR of $100 M_{\odot} \text{ yr}^{-1}.$

In Fig. 8 we reproduce the panels in figures 6 and 7 from Gouin et al. (2022) relating to the $z \approx 1.5$ and $z \approx 2$ structures in G073; we show the total SFR versus total stellar mass (i.e., the sum of all the galaxies within the cylinder) of all 30 simulated structures, and the total number of galaxies versus total stellar mass for the same simulated sample. We also show the same quantities for the observed galaxies as reported in Kneissl et al. (2019). Gouin et al. (2022) selected one of the 30 simulated structures that best matched the observations (highlighted in red), and we show individual SFRs and stellar masses of these specific simulated structures compared to the galaxies from Kneissl et al. (2019). Gouin et al. (2022) conclude that the TNG300 simulation is able to reproduce the PHZ selection, and that the simulated structures are comparable to the observations.

With our new ALMA observations spectroscopically confirming six galaxies around $z \approx 1.5$ and five galaxies around $z \approx 2,$ we would like to ask if the conclusions from Gouin et al. (2022) concerning G073 have changed. In Fig. 8 we therefore update the observed data points with values derived in this work. We find that the total observed SFR within the $z \approx 1.5$ structure increases while the total stellar mass decreases, although not substantially, while the $z \approx 2$ structure is in good agreement. The properties of the individual galaxies within G073 also remain consistent with the simulated structures selected by Gouin et al. (2022) to be the most similar to the observations from Kneissl et al. (2019).

Regarding the fates of the most star-forming halos found in the TNG300 simulation, Gouin et al. (2022) found that 60–70% of the simulated structures (which spanned a redshift range of 1.3 to 3.0) evolved into $> 10^{15} M_{\odot}$ galaxy clusters by redshift 0. Moreover, they found that protoclusters with more star-forming galaxies and with that star formation evenly spread across the galaxies (i.e., systems without a single extremely luminous galaxy alongside a number of faint galaxies) are more likely to become clusters by $z = 0.$ This is roughly in line with our observations, so we conclude that the results from Gouin et al. (2022) suggest a high probability that both structures in G073 will ultimately evolve into a galaxy clusters.

Lastly, we can speculate on the current masses of the G073 systems by scaling our estimated stellar masses to dark matter halo masses and adding them up. Behroozi et al. (2013) provide a fitting function scaling halo mass to stellar mass as a function of redshift, calibrated to a large body of observational constraints. Using their best-fit function, for the $z = 1.5$ structure we find $M_{\text{star}}/M_{\text{halo}} = 0.020\text{--}0.025$ and a total dark matter halo mass of $\approx 1 \times 10^{13} M_{\odot}.$ For the $z = 2$ structure we find $M_{\text{star}}/M_{\text{halo}} = 0.007\text{--}0.026$ and a total dark matter halo mass of $\approx 4 \times 10^{13} M_{\odot}.$

While these values are nowhere near the mass of a redshift 0 galaxy cluster, it is worth emphasizing that our line luminosity limits are modest. For example, van der Burg et al. (2013) fit Schechter functions to a sample of 10 spectroscopically-confirmed galaxy clusters around $z \approx 1,$ splitting the sources into a sample of star-forming galaxies and a sample of quiescent galaxies. Using their fit to the star-forming galaxies, and assuming we are only sensitive to galaxies with stellar masses $\geq 1 \times 10^{10} M_{\odot},$ we find that we would expect to find about 4 times more galaxies with stellar masses $> 10^9 M_{\odot}$ than with stellar masses $> 10^{10} M_{\odot}$ (corresponding to a total of about 25 galaxies in each system). This is again not enough mass to account for

$10^{15} M_{\odot}$, but growth through accretion outside of the field-of-view is expected.

6.2. Environmental effects on protocluster galaxies around redshift 1.5

To investigate possible environmental effects on the gas properties of $z \approx 2$ cluster and protocluster galaxies, we derive the field-relative gas depletion timescales and gas-to-stellar mass ratios by dividing the measured values from our sample and the collection from the literature by those of coeval field galaxies obtained through the Liu et al. (2019) scaling relations. The predicted field values are calculated using the redshift and the stellar mass of each source and ignoring corrections related to offsets to the main sequence. The broad range of stellar masses (about $(0.5\text{--}17) \times 10^{10} M_{\odot}$ or 1.5 dex span) and of SFRs (about $3\text{--}600 M_{\odot} \text{ yr}^{-1}$, or 2.3 dex span) of the G073 sources, combined with the cluster members, allows us to investigate possible dependencies with these parameters. The properties relative to field galaxies are shown as a function of SFR and stellar mass in Fig. 9.

We find that 51% of the cluster and protocluster members and 30% of the G073 sources have gas-to-stellar mass ratios that are consistent with coeval field galaxies, while 39% and 70% have larger ratios, respectively. This is consistent with previous results which find that CO emitters in high- z clusters have field-like or enhanced molecular gas fractions (i.e., Noble et al. 2017; Rudnick et al. 2017; Hayashi et al. 2018). Interestingly, the excess in gas fraction is observed at all masses, but there seems to be a mild trend with SFR. Although these results might suffer from a bias in favour of gas rich galaxies, it is expected that high-density environments at high redshift favour cold gas buildup, and the systems with the highest gas fractions are also the most star-forming ones.

Regarding the relative gas depletion times, 60% of the G073 sources have shorter depletion times than field galaxies, compared to 47% for the sample from the literature. There is a trend in relative depletion timescale with SFR, although this is to be expected as the depletion timescale is proportional to the inverse of the SFR. There is also a potential trend in relative depletion timescale with M_{star} , where higher stellar mass corresponds to longer depletion timescale. This trend might be explained by the galaxy maturity level, where galaxies in an earlier evolutionary phase have smaller stellar masses, larger star-forming efficiencies and higher gas-to-stellar mass ratios.

6.3. The nature of $850 \mu\text{m}$ -bright sources in PHz fields

It is also worth discussing the fact that no SCUBA-2-selected sources appear to be in the redshift 1.5 or 2 structures. These sources all have $S_{850} > 7$ mJy (and three have $S_{850} > 8$ mJy), and were part of a larger study of 61 PHz fields followed up by SCUBA-2 (MacKenzie et al. 2017). Of these 61 fields, 51 were protocluster candidates (so not strong gravitational lenses), and ultimately contained a factor of 6 enhancement in number density for sources above 8 mJy compared to blank-field surveys. This implied that the PHz objects at least contain projected overdensities of sources at $850 \mu\text{m}$ on the sky. MacKenzie et al. (2017) also fitted for photometric redshifts using the three *Herschel*-SPIRE bands and photometry at $850 \mu\text{m}$ from SCUBA-2, specifically finding photometric redshifts ≥ 2.5 for the four sources followed up in our programme (although with large un-

certainties) – effectively consistent with one of these sources being at $z = 2.6$.

Despite the fact that G073 contains statistically more $850 \mu\text{m}$ -bright sources than the field, they appear to be at higher redshifts than the two structures making up this field that we have studied in this work. This suggests a possibility that there are in fact three (or more) protoclusters along the line of sight, although this remains to be confirmed.

7. Summary and conclusions

We have used ALMA to search for $z \approx 1.5$ and $z \approx 2$ protocluster members in the *Planck*-selected field G073. In eight pointings targeting bright and red *Herschel*-SPIRE sources and four pointings targeting high S/N SCUBA-2 sources across the field, we have identified 27 individual galaxies through a combination of continuum and line emission, confirming six spectroscopic redshifts around $z \approx 1.5$ and five spectroscopic redshifts around $z \approx 2$. We have also found that the SCUBA-2 sources are not part of either of these protoclusters, instead likely lying in a more distant structure (or structures) at $z > 2.5$.

By fitting near-IR ($\sim 1 \mu\text{m}$) and far-IR (up to 2 mm) photometry to our sources, we derived star-formation rates and stellar masses, and we have also estimated gas masses using the CO and C_I line detections from our ALMA programme. Four galaxies are considered starbursts (having SFRs a factor of 4 larger than the MS), and the average gas-to-stellar mass ratio ($\mu_{\text{gas}} = M_{\text{gas}}/M_{\text{star}}$) of our protocluster galaxies is higher than typical scaling relations for field galaxies.

We have compared our more detailed view of G073 to the TNG300 simulation by updating the results from Gouin et al. (2022) with spectroscopic redshift information. Our observations remain consistent with the simulated star-forming halos at high redshift selected from the simulation. Since about 60–70% of the simulated halos collapse into galaxy clusters by redshift zero, we conclude that the two structures uncovered in G073 are comparably likely to become clusters as well. We estimate the total dark matter halo mass in observed galaxies to be around $10^{13} M_{\odot}$ in each structure, although we speculate that there are still a factor of 4 more galaxies with stellar masses an order of magnitude below our detection threshold of $\sim 10^{10} M_{\odot}$.

We show that the two structures spectroscopically detected by our observations are separated by about 3' in projection on the sky. Relative to *Planck*'s 5' beam originally used to select this field, this is in-line with previous claims that at least some of the PHz objects are line-of-sight alignments (e.g. Flores-Cacho et al. 2016), and indeed the presence of an overdensity of SCUBA-2 sources at higher redshift could indicate that this field contains three or more protoclusters. While this poses an observational challenge for future follow-up studies of a statistically significant sample of PHz objects, it also provides the potential for extracting more information than achievable from typical single-system fields. For example, the upcoming ALMA receiver upgrade (Carpenter et al. 2023) will boost the facility's spectral coverage by a factor of 4, meaning that with short observations of single PHz fields (such as G073) we can spectroscopically identify several protoclusters. A modest observing programme targeting of order 10 PHz objects therefore has the potential to find dozens of protoclusters, easily providing powerful population statistics of a homogeneously-selected sample of star-forming protoclusters (and their embedded galaxies) around the peak of the star formation activity of the Universe.

Acknowledgements. This work was supported by the Natural Sciences and Engineering Research Council of Canada. M.P. thanks the UCSD Astron-

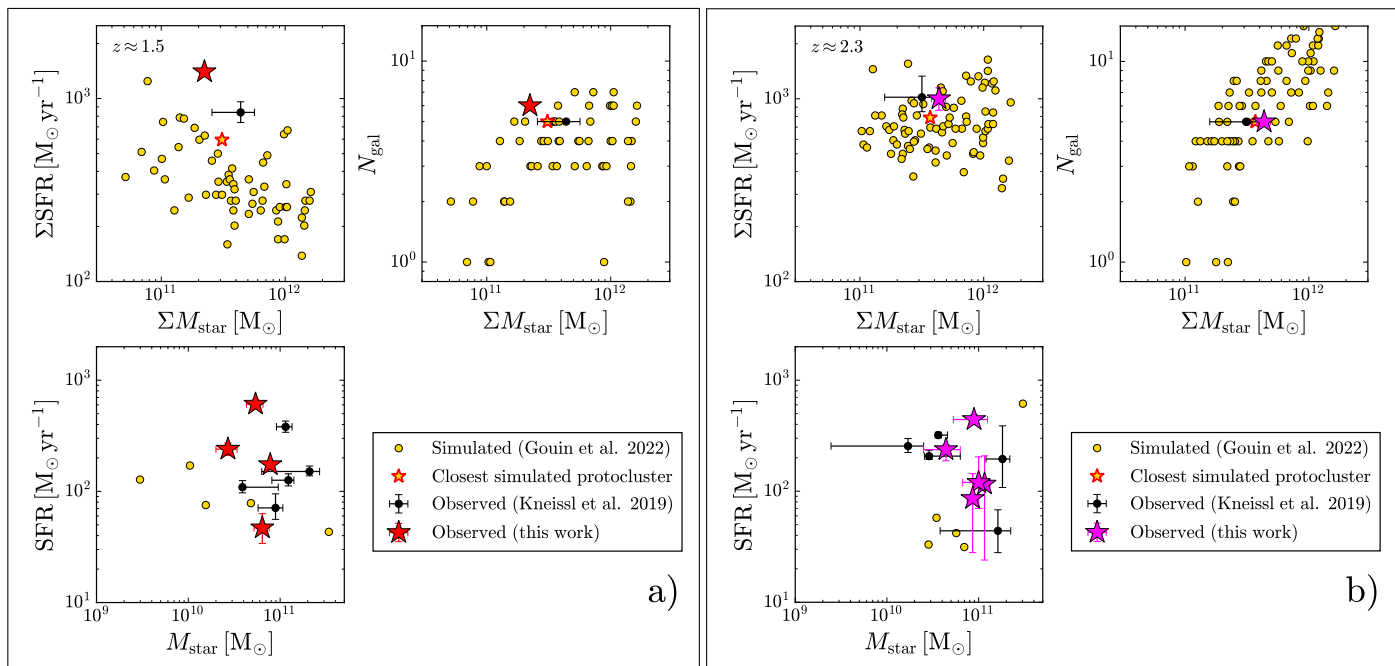


Fig. 8. Comparison of our results to the TNG300 simulation (Gouin et al. 2022) at (a) $z \approx 1.5$ and (b) $z \approx 2.3$. Top left in both panels: total protocluster SFR versus stellar mass for 30 simulated protoclusters (orange points), compared to previous observations based primarily on photometric redshifts (black point; Kneissl et al. 2019) and our new observations based only on spectroscopic redshifts (green points). The closest matching simulated halo selected by Gouin et al. (2022) is shown as the star. Top right in both panels: Same as previous panel but showing the total number of protocluster galaxies with $SFR > 10 M_{\odot} \text{ yr}^{-1}$ versus stellar mass. Bottom in both panels: SFR versus stellar mass for the individual galaxies in the closest-matching simulated halo (orange points), compared to previous observations (Kneissl et al. 2019) and this work.

omy & Astrophysics department for their warm hospitality. M.P. acknowledges financial support from INAF mini-grant 2023 ‘Galaxy growth and fuelling in high- z structures’. This paper makes use of the following ALMA data: ADS/JAO.ALMA#2018.1.00562.S and 2013.1.01173.S. ALMA is a partnership of ESO (representing its member states), NSF (USA) and NINS (Japan), together with NRC (Canada), MOST and ASIAA (Taiwan), and KASI (Republic of Korea), in cooperation with the Republic of Chile. The Joint ALMA Observatory is operated by ESO, AUI/NRAO and NAOJ. The National Radio Astronomy Observatory is a facility of the National Science Foundation operated under cooperative agreement by Associated Universities, Inc. The *Herschel* spacecraft was designed, built, tested, and launched under a contract to ESA managed by the *Herschel/Planck* Project team by an industrial consortium under the overall responsibility of the prime contractor Thales Alenia Space (Cannes), and including Astrium (Friedrichshafen) responsible for the payload module and for system testing at spacecraft level, Thales Alenia Space (Turin) responsible for the service module, and Astrium (Toulouse) responsible for the telescope, with in excess of a hundred subcontractors. The development of Planck has been supported by: ESA; CNES and CNRS/INSU-IN2P3-INP (France); ASI, CNR, and INAF (Italy); NASA and DoE (USA); STFC and UKSA (UK); CSIC, MICINN, JA, and RES (Spain); Tekes, AoF, and CSC (Finland); DLR and MPG (Germany); CSA (Canada); DTU Space (Denmark); SER/SSO (Switzerland); RCN (Norway); SFI (Ireland); FCT/MCTES (Portugal); and PRACE (EU). This work is based in part on observations made with the *Spitzer* Space Telescope, which is operated by the Jet Propulsion Laboratory, California Institute of Technology under a contract with NASA. Based in part on observations obtained with WIRCam, a joint project of CFHT, Taiwan, Korea, Canada, France, and the Canada-France-Hawaii Telescope (CFHT) which is operated by the National Research Council (NRC) of Canada, the Institut National des Sciences de l’Univers of the Centre National de la Recherche Scientifique of France, and the University of Hawaii. Based in part on observations made at James Clerk Maxwell Telescope (JCMT) with SCUBA-2. The JCMT is operated by the Joint Astronomy Centre on behalf of the Science and Technology Facilities Council of the United Kingdom, the Netherlands Organisation for Scientific Research, and the National Research Council of Canada.

Data availability

All of the data presented in this paper are publicly available. The ALMA data can be found under the two programmes

2013.1.01173.S (PI: R. Kneissl) and 2018.1.00562.S (PI: R. Hill). The *Spitzer* data are from Program ID 11004 (PI: H. Dole) and the CFHT data are from Proposal IDs 13BF12 and 14BF08 (PI: H. Dole).

References

- Alberts, S., Pope, A., Brodwin, M., et al. 2016, *ApJ*, 825, 72
 Amorín, R., Muñoz-Tuñón, C., Aguerri, J. A. L., & Planesas, P. 2016, *A&A*, 588, A23
 Andreon, S. 2003, *A&A*, 409, 37
 Aravena, M., Carilli, C. L., Salvato, M., et al. 2012, *MNRAS*, 426, 258
 Balogh, M. L., Navarro, J. F., & Morris, S. L. 2000, *ApJ*, 540, 113
 Behroozi, P. S., Wechsler, R. H., & Conroy, C. 2013, *ApJ*, 770, 57
 Birkin, J. E., Weiss, A., Wardlow, J. L., et al. 2021, *MNRAS*, 501, 3926
 Bolatto, A. D., Wolfire, M., & Leroy, A. K. 2013, *ARA&A*, 51, 207
 Bond, J. R., Kofman, L., & Pogosyan, D. 1996, *Nature*, 380, 603
 Boquien, M., Burgarella, D., Roehlly, Y., et al. 2019, *A&A*, 622, A103
 Boselli, A., Epinat, B., Contini, T., et al. 2019, *A&A*, 631, A114
 Bothwell, M. S., Aguirre, J. E., Aravena, M., et al. 2017, *MNRAS*, 466, 2825
 Brodwin, M., Stanford, S. A., Gonzalez, A. H., et al. 2013, *ApJ*, 779, 138
 Bruzual, A. G. & Charlot, S. 2003, *MNRAS*, 344, 1000
 Buat, V., Ciesla, L., Boquien, M., Małek, K., & Burgarella, D. 2019, *A&A*, 632, A79
 Calzetti, D., Armus, L., Bohlin, R. C., et al. 2000, *ApJ*, 533, 682
 Carpenter, J., Brogan, C., Iono, D., & Mroczkowski, T. 2023, in *Physics and Chemistry of Star Formation: The Dynamical ISM Across Time and Spatial Scales*, ed. V. Ossenkopf-Okada, R. Schaaf, I. Breloy, & J. Stutzki, 304
 CASA Team, Bean, B., Bhatnagar, S., et al. 2022, *PASP*, 134, 114501
 Casey, C. M. 2012, *MNRAS*, 425, 3094
 Casey, C. M., Cooray, A., Capak, P., et al. 2015, *ApJ*, 808, L33
 Casey, C. M., Narayanan, D., & Cooray, A. 2014, *Phys. Rep.*, 541, 45
 Castignani, G., Jablonka, P., Combes, F., et al. 2020, *A&A*, 640, A64
 Chabrier, G. 2003, *PASP*, 115, 763
 Chapman, S. C., Bertoldi, F., Smail, I., et al. 2015, *MNRAS*, 449, L68
 Chapman, S. C., Blain, A., Ibata, R., et al. 2009, *ApJ*, 691, 560
 Chiang, Y.-K., Overzier, R. A., Gebhardt, K., et al. 2015, *ApJ*, 808, 37
 Coogan, R. T., Daddi, E., Sargent, M. T., et al. 2018, *MNRAS*, 479, 703
 Cortese, L., Fritz, J., Bianchi, S., et al. 2014, *MNRAS*, 440, 942
 D’Amato, Q., Gilli, R., Prandoni, I., et al. 2020, *A&A*, 641, L6

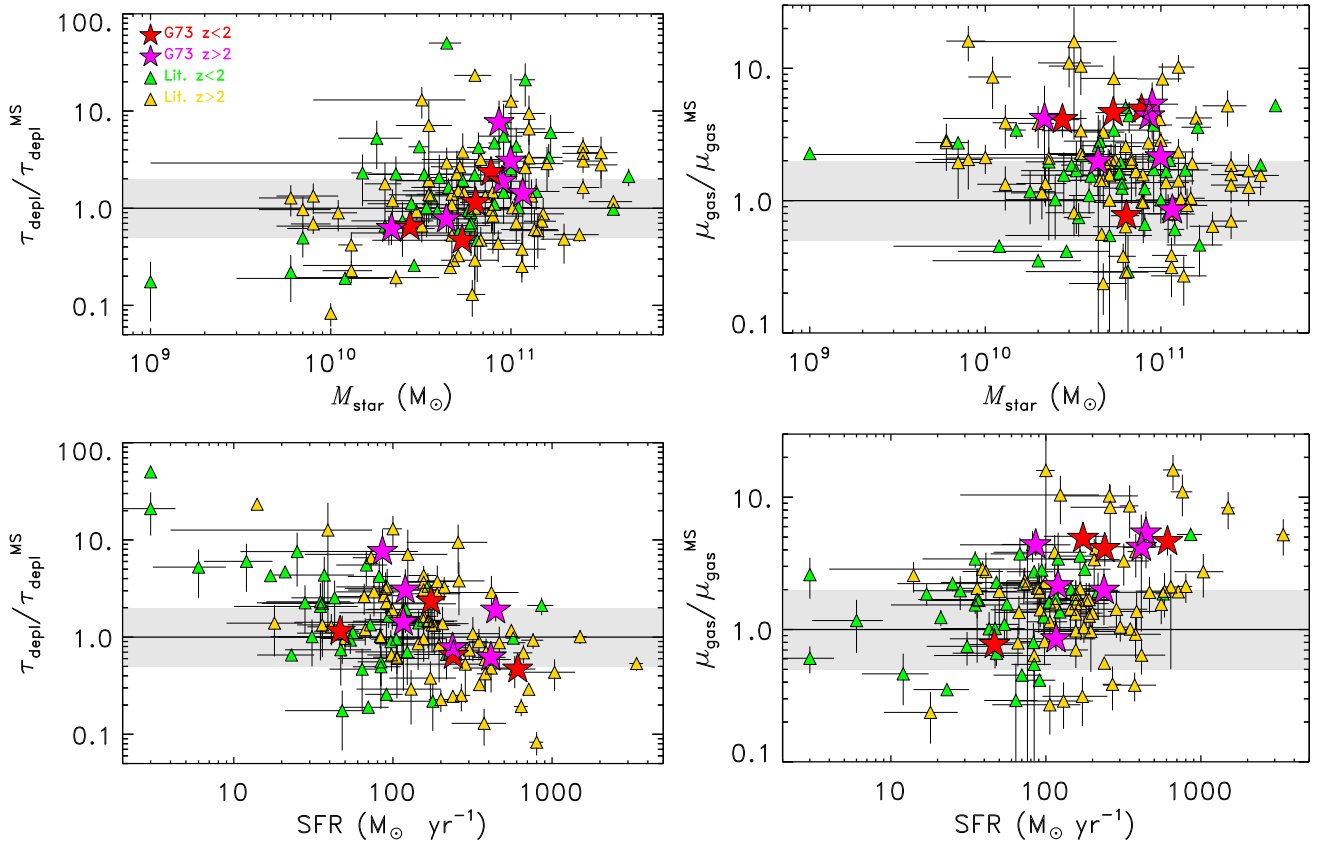


Fig. 9. Gas depletion timescales (left) and gas-to-stellar mass ratios (right) of cluster galaxies relative to the predicted gas properties as a function of stellar mass (top) and of SFR (bottom). The predicted properties are estimated for each individual source given its redshift and stellar mass assuming the scaling relations derived for field galaxies by Liu et al. (2019). Symbols are as in Fig. 6. The black solid line represents the Liu et al. (2019) scaling relation for τ_{depl} and $\mu_{\text{gas}} = M_{\text{gas}}/M_{\text{star}}$ with a scatter of 0.3 dex (grey shaded regions). About half of the CO-emitters in this work is characterized by higher gas-to-stellar mass ratios, which is also seen in the other cluster samples. On the other hand, most of the galaxies in G073 have depletion times consistent with the field.

- D’Amato, Q., Prandoni, I., Brienza, M., et al. 2021, *Galaxies*, 9, 115
Dannerbauer, H., Kurk, J. D., De Breuck, C., et al. 2014, *A&A*, 570, A55
Dannerbauer, H., Lehnert, M. D., Emonts, B., et al. 2017, *A&A*, 608, A48
Draine, B. T., Aniano, G., Krause, O., et al. 2014, *ApJ*, 780, 172
Dunne, L., Maddox, S. J., Vlahakis, C., & Gomez, H. L. 2021, *MNRAS*, 501, 2573
Ellis, R. S., Smail, I., Dressler, A., et al. 1997, *ApJ*, 483, 582
Fakhouri, O. & Ma, C.-P. 2009, *MNRAS*, 394, 1825
Fassbender, R., Nastasi, A., Böhringer, H., et al. 2011, *A&A*, 527, L10
Flores-Cacho, I., Pierini, D., Soucail, G., et al. 2016, *A&A*, 585, A54
Gavazzi, G., Boselli, A., Mayer, L., et al. 2001, *ApJ*, 563, L23
Genzel, R., Tacconi, L. J., Combes, F., et al. 2012, *ApJ*, 746, 69
Genzel, R., Tacconi, L. J., Lutz, D., et al. 2015, *ApJ*, 800, 20
Gómez-Guijarro, C., Riechers, D. A., Pavesi, R., et al. 2019, *ApJ*, 872, 117
González-López, J., Bauer, F. E., Aravena, M., et al. 2017, *A&A*, 608, A138
González-López, J., Decarli, R., Pavesi, R., et al. 2019, *ApJ*, 882, 139
Gottlöber, S., Klypin, A., & Kravtsov, A. V. 2001, *ApJ*, 546, 223
Gouin, C., Aghanim, N., Dole, H., Polletta, M., & Park, C. 2022, *A&A*, 664, A155
Gunn, J. E. & Gott, J. Richard, I. 1972, *ApJ*, 176, 1
Gururajan, G., Bethermin, M., Sulzenauer, N., et al. 2023, *A&A*, 676, A89
Hagimoto, M., Bakx, T. J. L. C., Serjeant, S., et al. 2023, *MNRAS*, 521, 5508
Hayashi, M., Kodama, T., Koyama, Y., Tadaki, K.-i., & Tanaka, I. 2011, *MNRAS*, 415, 2670
Hayashi, M., Kodama, T., Koyama, Y., et al. 2010, *MNRAS*, 402, 1980
Hayashi, M., Tadaki, K.-i., Kodama, T., et al. 2018, *ApJ*, 856, 118
Hennawi, J. F., Prochaska, J. X., Cantalupo, S., & Arrigoni-Battaia, F. 2015, *Science*, 348, 779
Hilton, M., Lloyd-Davies, E., Stanford, S. A., et al. 2010, *ApJ*, 718, 133
Inoue, S., Takagi, T., Miyazaki, A., et al. 2021, *MNRAS*, 506, 84
Iverson, R. J., Swinbank, A. M., Smail, I., et al. 2013, *ApJ*, 772, 137
Jiang, L., Wu, J., Bian, F., et al. 2018, *Nature Astronomy*, 2, 962
Kauffmann, G. 1996, *MNRAS*, 281, 487
Kennicutt, R. C. & Evans, N. J. 2012, *ARA&A*, 50, 531
Kneissl, R., Polletta, M., Martinache, C., et al. 2019, *A&A*, 625, A96
Koyama, Y., Polletta, M. d. C., Tanaka, I., et al. 2021, *MNRAS*, 503, L1
Larson, R. B., Tinsley, B. M., & Caldwell, C. N. 1980, *ApJ*, 237, 692
Lee, M. M., Tanaka, I., Kawabe, R., et al. 2017, *ApJ*, 842, 55
Liu, D., Schinnerer, E., Groves, B., et al. 2019, *ApJ*, 887, 235
MacKenzie, T. P., Scott, D., Bianconi, M., et al. 2017, *MNRAS*, 468, 4006
Mei, S., Hatch, N. A., Amodeo, S., et al. 2023, *A&A*, 670, A58
Miller, T. B., Chapman, S. C., Aravena, M., et al. 2018, *Nature*, 556, 469
Muzzin, A., Wilson, G., Yee, H. K. C., et al. 2012, *ApJ*, 746, 188
Nantais, J. B., Muzzin, A., van der Burg, R. F. J., et al. 2017, *MNRAS*, 465, L104
Noble, A. G., McDonald, M., Muzzin, A., et al. 2017, *ApJ*, 842, L21
Noble, A. G., Muzzin, A., McDonald, M., et al. 2019, *ApJ*, 870, 56
Noirot, G., Stern, D., Mei, S., et al. 2018, *ApJ*, 859, 38
Oteo, I., Ivison, R. J., Dunne, L., et al. 2018, *ApJ*, 856, 72
Peng, Y., Maiolino, R., & Cochrane, R. 2015, *Nature*, 521, 192
Planck Collaboration VI. 2020, *A&A*, 641, A6
Planck Collaboration XXVII. 2015, *A&A*, 582, A30
Planck Collaboration XXXIX. 2016, *A&A*, 596, A100
Pokhrel, R., Gutermuth, R., Ali, B., et al. 2016, *MNRAS*, 461, 22
Polletta, M., Soucail, G., Dole, H., et al. 2021, *A&A*, 654, A121
Popesso, P., Concas, A., Cresci, G., et al. 2023, *MNRAS*, 519, 1526
Rodighiero, G., Daddi, E., Baronchelli, I., et al. 2011, *ApJ*, 739, L40
Rudnick, G., Hodge, J., Walter, F., et al. 2017, *ApJ*, 849, 27
Sargent, M. T., Daddi, E., Béthermin, M., et al. 2014, *ApJ*, 793, 19
Sillassen, N. B., Jin, S., Magdis, G. E., et al. 2024, *arXiv e-prints*, arXiv:2407.02973
Solomon, P. M., Downes, D., Radford, S. J. E., & Barrett, J. W. 1997, *ApJ*, 478, 144
Steidel, C. C., Adelberger, K. L., Shapley, A. E., et al. 2000, *ApJ*, 532, 170
Tacconi, L. J., Genzel, R., Saintonge, A., et al. 2018, *ApJ*, 853, 179
Tacconi, L. J., Genzel, R., Smail, I., et al. 2008, *ApJ*, 680, 246
Tadaki, K.-i., Kodama, T., Hayashi, M., et al. 2019, *PASJ*, 71, 40
Tadaki, K.-i., Kodama, T., Ota, K., et al. 2012, *MNRAS*, 423, 2617
Tadaki, K.-i., Kodama, T., Tamura, Y., et al. 2014, *ApJ*, 788, L23
Tran, K.-V. H., Nanayakkara, T., Yuan, T., et al. 2015, *ApJ*, 811, 28
Tran, K.-V. H., Papovich, C., Saintonge, A., et al. 2010, *ApJ*, 719, L126
van der Burg, R. F. J., Muzzin, A., Hoekstra, H., et al. 2013, *A&A*, 557, A15
Wang, T., Elbaz, D., Daddi, E., et al. 2018, *ApJ*, 867, L29
Webb, T., Noble, A., DeGroot, A., et al. 2015, *ApJ*, 809, 173
Wolfire, M. G., Hollenbach, D., & McKee, C. F. 2010, *ApJ*, 716, 1191

Appendix A: ALMA spectra

Here we show continuum maps, moment-0 maps, and spectra of the galaxies observed in G073 (Fig. A.1). For each source, the upper panels show $3'' \times 3''$ cutouts. Continuum images obtained by stacking all channels containing no line emission are shown as the background, and overlaid are corresponding continuum contours starting at 2σ and increasing in steps of 3σ . We also show line emission moment-0 contours from stacking all channels between -3σ and 3σ (where σ is the standard deviation of the best-fitting linewidth). These contours also start at 2σ and increase in steps of 3σ .

In the lower panels we show our continuum-subtracted LSB and USB spectra. The best-fitting Gaussian functions are plotted on top of the spectra. The shaded region ranges from -3σ to 3σ , corresponding to the range used to calculate line strengths.

Appendix B: Near-IR photometric data

Here we provide the near-IR photometry used to fit SEDs and derive physical properties of the galaxies in G073. The J and K_s -band data are from WIRcam on the CFHT, and the $3.6\mu\text{m}$ and $4.5\mu\text{m}$ data are from *Spitzer*-IRAC.

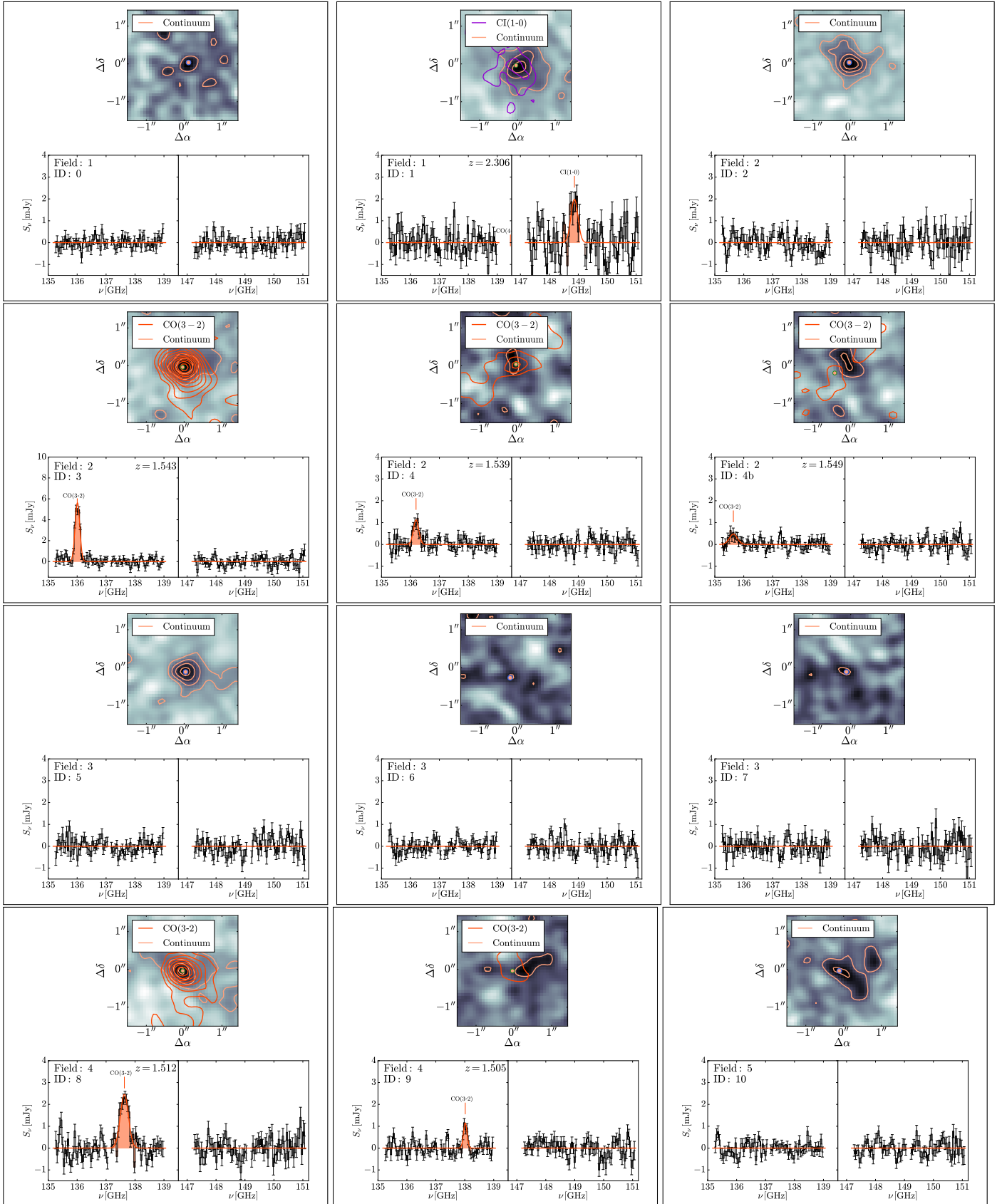


Fig. A.1. ALMA Band 4 cutouts and spectra for all sources in G073. The upper panels show $3'' \times 3''$ cutouts, with continuum images in the background highlighted by orange contours starting at 2σ and increasing in steps of 3σ . For sources with line detections, moment-0 contours (red) are overlaid following the same steps. The lower panels show the continuum-subtracted LSB and USB spectra, with the best-fitting Gaussian functions plotted over the raw data and the shaded regions indicating the integration range used to measure the line strengths.

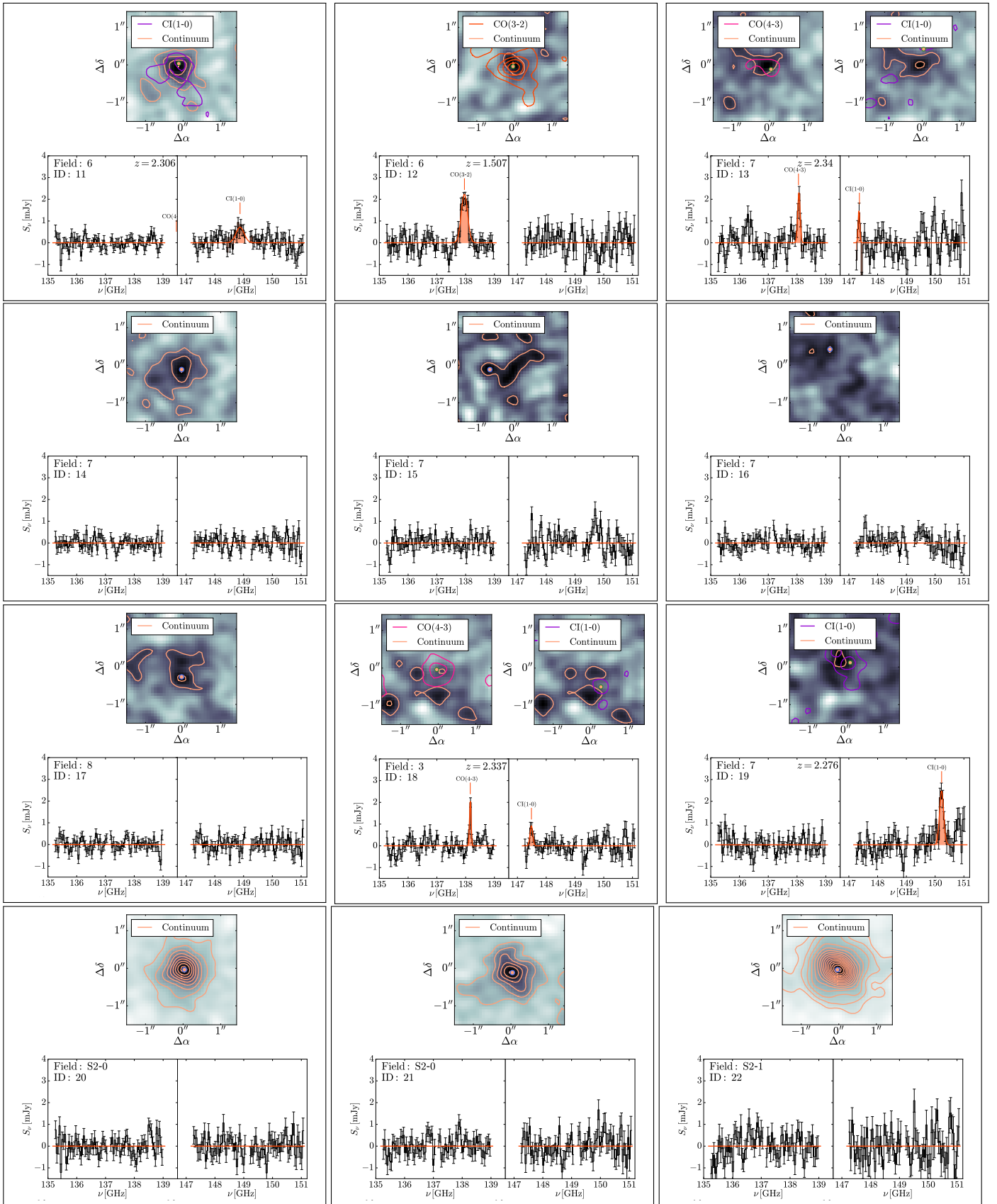


Fig. A.1. Continued.

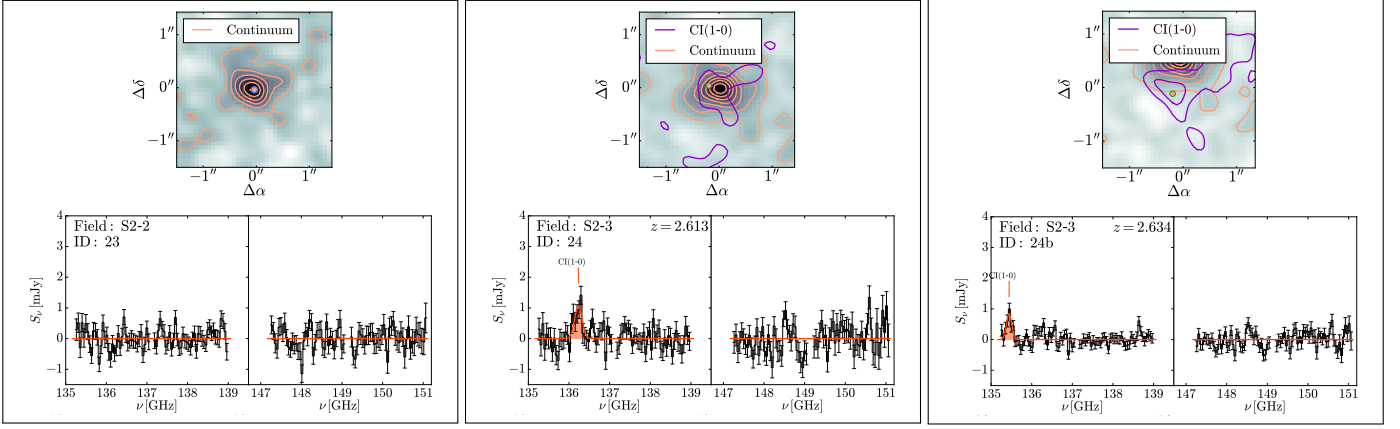


Fig. A.1. Continued.

Table B.1. Near- and mid-IR flux densities of the Band 4+6 continuum galaxies found in G073.

Field ID	S_J [μJy]	S_{K_s} [μJy]	$S_{3,6}$ [μJy]	$S_{4,5}$ [μJy]
1 0	24.98 ± 0.44	77.15 ± 0.92	137.41 ± 0.82	114.32 ± 1.08
1 1	<1.10	<4.37	14.37 ± 0.83	20.30 ± 1.11
2 2	<1.10	<4.37	5.47 ± 0.92	7.86 ± 1.27
2 3	8.61 ± 0.46	18.28 ± 1.47	45.30 ± 0.90	57.37 ± 1.27
2 4	<1.10	<4.37	6.53 ± 0.88	8.03 ± 1.02
3 5	6.21 ± 0.44	18.19 ± 0.92	39.96 ± 0.83	49.79 ± 1.11
3 6	2.06 ± 0.44	4.60 ± 0.93	16.00 ± 0.84	22.13 ± 1.12
3 7	<1.10	<4.37	5.72 ± 0.85	6.24 ± 1.11
3 18	2.09 ± 0.45	8.82 ± 0.93	17.18 ± 0.84	19.61 ± 1.11
4 8	8.40 ± 0.44	20.31 ± 0.92	49.19 ± 0.82	63.65 ± 1.10
4 9	2.78 ± 0.44	6.66 ± 0.92	20.23 ± 0.83	23.34 ± 1.12
5 10	16.31 ± 0.44	34.07 ± 0.92	58.24 ± 2.85	52.33 ± 3.03
6 11	<1.10	6.35 ± 0.96	14.22 ± 0.88	16.78 ± 1.17
6 12	2.25 ± 0.46	10.30 ± 0.93	23.28 ± 0.87	32.22 ± 1.16
7 13	<1.10	4.68 ± 1.10	10.40 ± 1.67	14.61 ± 1.92
7 14	<1.10	<4.37	2.95 ± 1.68	3.40 ± 1.93
7 15	<1.10	<4.37	<5.03	<5.78
7 16	6.27 ± 0.54	13.69 ± 1.01	20.54 ± 1.67	13.60 ± 1.92
7 19	3.90 ± 0.30	8.20 ± 0.54	17.19 ± 1.67	16.89 ± 2.13
8 17	5.48 ± 0.50	19.13 ± 1.00	40.68 ± 0.87	40.01 ± 1.28
S2-0 20	<1.10	<4.37	<5.03	<5.78
S2-0 21	<1.10	<4.37	5.08 ± 0.83	8.35 ± 1.11
S2-1 22	<1.10	<4.37	3.76 ± 0.91	4.67 ± 1.31
S2-2 23	1.44 ± 0.45	4.28 ± 0.92	14.52 ± 0.84	17.54 ± 1.11
S2-3 24	<1.10	<4.37	2.08 ± 1.08	3.00 ± 1.74
S2-3 25	<1.10	<4.37	2.08 ± 1.08	3.00 ± 1.74

Notes. Upper limits correspond to 5σ .